


RESEARCH PAPER



Engineered bacteria as an orally administered anti-viral treatment and immunization system

Nitin S. Kamble, Shindu Thomas, Tushar Madaan, Nadia Ehsani, Saqib Sange, Kiersten Tucker, Alexis Muhumure, Sarah Kunkler, and Nalinikant Kotagiri 

Division of Pharmaceutical Sciences, James L. Winkle College of Pharmacy, University of Cincinnati, Cincinnati, OH, USA

ABSTRACT

The emergence of new viral pathogens necessitates innovative antiviral therapies and vaccines. Traditional approaches, such as monoclonal antibodies and vaccines, are often hindered by resistance, limited effectiveness, and high costs. Here, we develop an engineered probiotic-based antiviral platform using *Escherichia coli* Nissle 1917 (EcN), capable of providing both mucosal and systemic immunity via oral administration. EcN was engineered to display anti-spike nanobodies or express the Spike-Receptor Binding Domain on its surface. Our findings reveal that EcN with nanobodies effectively inhibits the interaction between spike protein-expressing pseudoviruses and the ACE2 receptor. Furthermore, we observed the translocation of nanobodies to distant organs, facilitated by outer membrane vesicles (OMVs). The oral administration of EcN expressing spike proteins induced a robust immune response characterized by the production of both IgG and IgA, antibodies that blocked the pseudovirus-ACE2 interaction. While SARS-CoV-2 served as a model, this versatile probiotic platform holds potential for developing customizable biotherapeutics against a wide range of emerging pathogens such as influenza virus or respiratory syncytial virus (RSV) by engineering EcN to express viral surface protein or neutralizing nanobodies demonstrating its versatility as a next-generation mucosal vaccine strategy.

ARTICLE HISTORY

Received 29 January 2025
Revised 5 April 2025
Accepted 24 April 2025

KEYWORDS



Engineered probiotics; live antiviral nanobody therapeutics; live antiviral vaccines; mucosal and systemic immunity; outer membrane vesicles (OMVs)


Introduction

The use of engineered probiotics and bacteria for therapeutic delivery has evolved into a promising field, particularly for immunotherapy. Early research focused on leveraging the beneficial properties of commensal bacteria, known for their natural ability to colonize the gastrointestinal (GI) tract and interact with the host immune system.¹ Probiotics have traditionally been utilized to restore healthy gut microbiota, aiding digestion and modulating immune responses.² Additionally, probiotics have demonstrated a remarkable potential in reducing the risk and severity of various viral respiratory tract infections, as well as in preventing bacterial and viral infections, including sepsis and gastroenteritis.^{3–5} Oral therapeutic formulations harness the gut's immune system to generate comprehensive systemic and mucosal immune responses, resulting in robust and persistent immunity.⁶

Symbiotic native bacteria, having coevolved with humans, offer a promising avenue for developing innovative platforms for vaccines and therapeutics.^{7,8} The oral administration of such delivery systems for therapeutics and vaccines provides numerous benefits, including self-administration, enhanced safety, improved patient compliance, and streamlined manufacturing and distribution processes, compared to injection-based approaches.^{9,10} An oral vaccine capable of efficiently delivering immunogens while simultaneously providing both mucosal and systemic immunity would be highly advantageous.^{9–11}

Engineered probiotics offer a promising alternative, capitalizing on the natural interactions between commensal microbes and the host immune system. Initial developments in this area concentrated on using engineered probiotics to deliver cytokines or anti-inflammatory agents to treat intestinal diseases, such as inflammatory

CONTACT Nalinikant Kotagiri  kotaginh@ucmail.uc.edu  Division of Pharmaceutical Sciences, James L. Winkle College of Pharmacy, University of Cincinnati, Cincinnati, OH 45267, USA

 Supplemental data for this article can be accessed online at <https://doi.org/10.1080/19490976.2025.2500056>

© 2025 The Author(s). Published with license by Taylor & Francis Group, LLC.

This is an Open Access article distributed under the terms of the Creative Commons Attribution-NonCommercial License (<http://creativecommons.org/licenses/by-nc/4.0/>), which permits unrestricted non-commercial use, distribution, and reproduction in any medium, provided the original work is properly cited. The terms on which this article has been published allow the posting of the Accepted Manuscript in a repository by the author(s) or with their consent.

bowel disease (IBD). For instance, *Lactococcus lactis* was genetically modified to produce interleukin-10 (IL-10), an anti-inflammatory cytokine, within the gut.^{12,13} These early applications demonstrated that engineered bacteria could effectively modulate the local immune environment, providing therapeutic benefits and reducing inflammation.

The concept was later expanded to include vaccine delivery. Researchers explored the expression of viral proteins, like influenza hemagglutinin or rotavirus VP6, on the surface of *Lactobacillus* species to stimulate mucosal and systemic immune responses.¹⁴

More recent advancements have introduced the use of camelid heavy-chain-only antibody variable domains (VHHs), or nanobodies, which represent promising lead molecules for passive immunization.^{15–17} Furthermore, nanobodies provide a rapid production route for antiviral agents, owing to their small size, exceptional stability, and easy scalability using bacterial expression systems, laying the groundwork for their use in engineered probiotic systems.^{15,18}

The current study builds on these advancements by using *Escherichia coli* Nissle 1917 (EcN) as a delivery vehicle for both nanobodies and viral antigens, particularly for SARS-CoV-2, the virus responsible for the COVID-19 pandemic.^{16,19} EcN is a naturally gut colonizing, well-characterized probiotic strain, commercially available as Mutaflor[®] which lacks virulence factors, thus making it safe for therapeutic applications. Unlike previous efforts where only active immunization strategy is used by expressing spike protein on bacteria cell surface,²⁰ this study integrates both passive and active immunization strategies. EcN was engineered to express anti-Spike protein nanobodies on its surface, providing immediate viral neutralization through passive immunity. Simultaneously, the expression of the spike protein on the surface is designed to elicit an active immune response, fostering long-term immunity. We designed fusion proteins to generate a spike protein coupled with bacterial Intimin and Lpp-OmpA, which would ensure stable tethering to the bacterial surface to amplify the immune response against the spike protein (Figure 1).^{9,21}

We postulated that surface expression of the nanobodies and antigen would enable the

utilization of bacterial outer membrane vesicles (OMVs) as a delivery system. OMVs are naturally secreted by Gram-negative bacteria like EcN and can carry a variety of biomolecules, including proteins and nucleic acids. In this study, OMVs were employed to transport nanobodies from the gut lumen to the systemic circulation, facilitating a comprehensive immune response.

Results

Surface expression of SARS-CoV-2 anti-spike glycoprotein nanobodies

We engineered a synthetic modular vector for the expression of SARS-CoV-2-specific nanobodies on the surface of EcN. Surface display allows for efficient antigen presentation of nanobodies, direct interaction with host cells and ensuring nanobody-mediated neutralization (Figure 2(a)). This vector included genetic elements for the surface display of anti-Spike nanobodies, incorporating Flag, Strep II tags, and TEV cleavage sites for detection and purification (Supplementary Figure S1, a-b, S2, a-b, Table S1). The vector was built on a J23105 plasmid backbone with a moderate-strength constitutive promoter to ensure stable nanobody production (Supplementary Figure S1, e).^{22,23} We selected two specific nanobodies, VHH72 and Ty1, targeting the Spike protein's receptor-binding domain (RBD). Both VHH72 and Ty1 nanobodies have been previously characterized to bind with sub-nanomolar dissociation constant (Kd) and picomolar-range affinity respectively, making them the most potent anti-RBD nanobodies identified.^{15,17,24} These nanobodies were synthesized using gene synthesis and codon optimization techniques. We then created nanobody constructs fused with Intimin (pIntimin-Ty1 and pIntimin-VHH72 (Supplementary Figure S1, a-b, S2, a-b, Table S1), a protein known for its cell surface anchoring capabilities, comprising a short N-terminal signal sequence, a LysM domain, and a β -barrel transmembrane segment.^{21,25,26} We introduced restriction sites in the plasmid for future modifications. Post-transformation into EcN, we confirmed the expression of these constructs through SDS-PAGE-Western immunanalysis. The successful expression of both pInt-

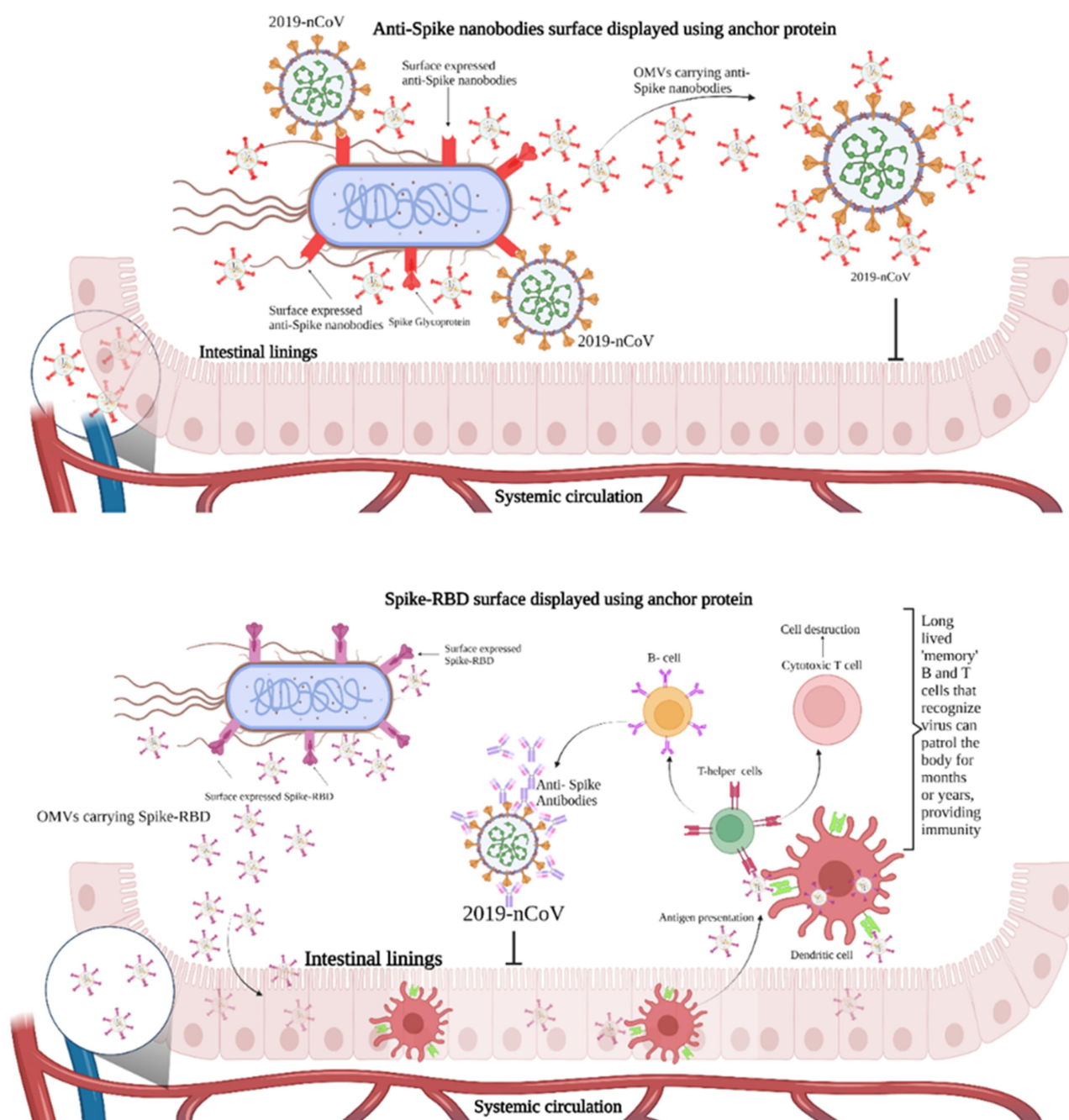


Figure 1. Engineered *EcN* serves as an oral anti-viral therapy and immunization platform against SARS-CoV-2. Top panel: engineered *EcN* display anti-spike nanobodies on their surface and release OMVs carrying nanobodies, neutralizing the virus in the gut and potentially entering systemic circulation. Bottom panel: engineered *EcN* express spike-RBD, stimulating antigen presentation by dendritic cells, activating B cells for antibody production and T cells for immune memory. This approach provides mucosal and systemic immunity against SARS-CoV-2.

Ty1 and pInt-VHH72 nanobodies was verified (Figure 2(b)) as shown with ~89.4 and ~90.5kDa bands, respectively. Similarly, we also explored the effect of surface tethering protein size on nanobody display. We used a smaller Lpp-OmpA hybrid surface display signal (Figure 2(c)), constructing

pLpp-OmpA-Ty1 and pLpp-OmpA-VHH72 (Supplementary Figure S1, c-d, S2, c-d, Table 1). Lpp-OmpA comprises a signal sequence, the N-terminal of lipoprotein (Lpp), and the remaining OmpA protein, known for stable surface expression (Figure 2(c)).^{27–30} Fusion of Ty1 and VHH72

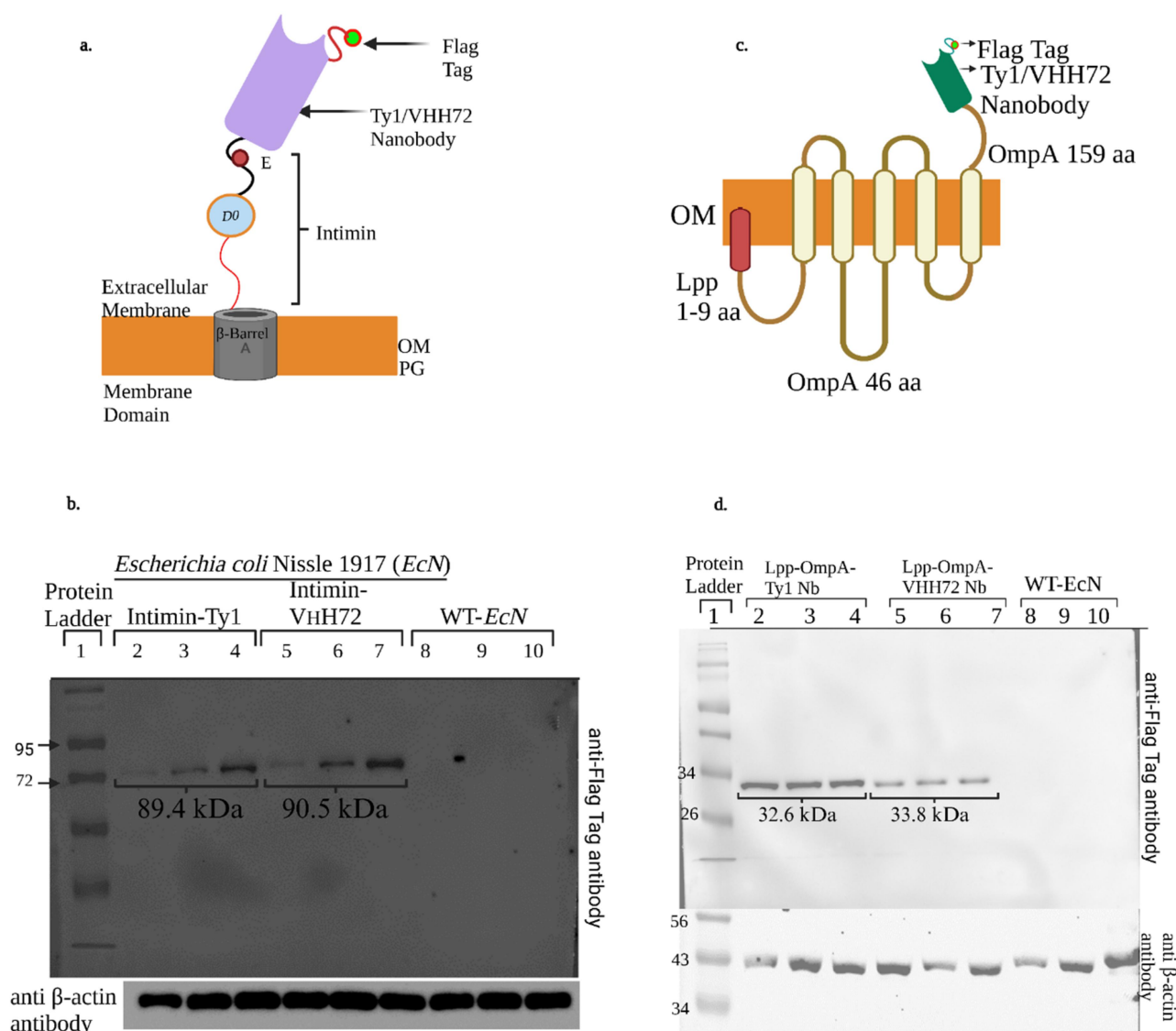


Figure 2. Modular constructs for surface displaying nanobodies on the bacterial cell surface and their validation with Western blot analysis. Schematic displaying nanobodies (Ty1 and VHH72) on the cell surface anchored with intimin protein (a). The nanobody expression of plnt-Ty1 and plnt-VHH72 was confirmed with Western blot analysis (b) showing 89.4 and 90.5 kDa bands compared to absence of bands in wells loaded with EcN-expressing empty plasmids. Schematic displaying nanobodies (Ty1 and VHH72) on the cell surface anchored with Lpp-OmpA protein (c). The nanobody expression of pLpp-OmpA-Ty1 and pLpp-OmpA-VHH72 was confirmed with Western blot analysis (d) showing 32.6 and 33.8 kDa bands compared to absence of bands in wells loaded with EcN-expressing empty plasmids. Blots were developed with anti-flag tag antibody, and anti-β-actin antibody using the ChemiDoc™ imaging system (BioRad). Schematics were drawn using biorender (nb-nanobody).

nanobodies to Lpp-OmpA's C-terminus led to successful expression, confirmed by Western blot (Figure 2(d)).

We further confirmed these nanobody expressions with mass spectrometry-based proteomics analysis, in which, proteins are digested into peptides which are then identified and quantified. The number of unique peptides identified for a protein correlates with its abundance. The successful expression of both pInt-Ty1 and pInt-VHH72

nanobodies was verified. Proteomics analysis further validated the expression of Intimin-fused nanobodies, with ~37 unique peptides identified for pInt-Ty1 (Supplementary Figure S2, e, Table S2). Proteomics analysis also revealed ~11 unique peptides for pLpp-OmpA-Ty1 (Supplementary Figure S2, f, Table S3). Furthermore, we generated a total ion chromatogram (TIC) from mass spectral peaks and estimated protein abundance from tandem MS spectra (Supplementary Figure S3, a-d).³¹

Principal component analysis (PCA) was used to simplify the spectral dataset (Supplementary Figure S3, e, f).

Bacterial surface-anchored anti-spike nanobodies inhibit spike and ACE2 receptor interaction

Our experiments focused on evaluating the binding efficiency of nanobodies displayed on EcN to the SARS-CoV-2 spike protein. We employed a fluorescence-based functional assay to confirm this interaction. We chose pseudovirus-ACE2 system as it allows us to safely study SARS-CoV-2 Spike-ACE2 interactions in a BSL-2 setting, avoiding the need for live virus (BSL-3 containment). Pseudoviruses mimic the entry mechanism of SARS-CoV-2 by displaying the Spike protein, making them a reliable tool to assess nanobody-mediated neutralization, thus showing functional relevance. Both Ty1 and VHH72 nanobodies are known to bind to the RBD of the SARS-CoV-2 spike protein.^{15,17,18} In our tests, we utilized the recombinant SARS-CoV-2 spike protein (encompassing S1 and S2 domains), with nanobodies primarily targeting the S1 domain. As a comparative measure, we also used a SARS-CoV-2 S protein S2 antibody that binds selectively to the S2 domain (Supplementary Figure S4-S5). This interaction was visualized using an AlexaFluor®647-conjugated anti-mouse antibody. Our results showed that EcN cells expressing pInt-Ty1 (Figure 3(a)), pInt-VHH72 (Figure 3(b)), and pLpp-OmpA-Ty1 (Figure 3(c)) nanobodies exhibited significantly stronger binding to the spike protein than control EcN cells. However, EcN expressing pLpp-OmpA-VHH72 did not show a notable difference in binding compared to the control (Figure 3(d)). Additionally, an indirect ELISA (Figure 3(e)) revealed that Ty1 nanobodies, irrespective of being anchored to Intimin or Lpp-OmpA, bound significantly to the SARS-CoV-2 spike protein, while VHH72 nanobodies did not show a significant difference from the control (Figure 3(f)). This data indicates that our synthetic constructs, employing Intimin and Lpp-OmpA surface display signals on the bacterial cell membrane, exhibit enhanced binding to the spike protein compared to the control *EcN*. Furthermore, we assessed the ability of the surface-displayed

nanobodies to block the interaction between the spike-RBD and the ACE2 receptor. All four nanobody constructs effectively inhibited this interaction, with the inhibition strength ranking as follows: pLpp-OmpA-VHH72 > pInt-Ty1 > pLpp-OmpA-Ty1 > pInt-VHH72 (Figure 3(g-j)). This trend might be due to steric hindrance and nanobody orientation. Lpp-OmpA anchors the nanobody closer to the outer membrane surface but still provides some flexibility for antigen binding, whereas Intimin extends further from the bacterial surface, which may be beneficial for accessibility but could also introduce instability in certain constructs. The ranking suggests that Lpp-OmpA provides a more stable and accessible presentation of VHH72 compared to Intimin. These findings suggest that EcN displaying these nanobodies can successfully block the interaction between the SARS-CoV-2 spike protein and the ACE2 receptor. The observed differences can be attributed to the difference in the sizes of the anchor proteins, where Intimin, being a larger protein, has the ability to project these domains well outside the bacterial cell surface. The large, projecting domain of Intimin can interact more freely with the external environment, making it ideal for presenting proteins that require significant exposure for immune recognition or interaction with other molecules.

Serum nanobodies from mice inhibit pseudovirus and ACE2 interaction

Encouraged by our initial success with *in vitro* binding and receptor inhibition, we next explored the *in vivo* efficacy of our engineered EcN expressing pInt-Ty1 nanobodies (EcN-Ty1). We orally administered EcN-Ty1 in mice every day for 4 consecutive days, with the objective of colonizing their gut and assessing the translocation of nanobodies into the systemic circulation. Blood was drawn 24 hours after every dose. Western blot analysis of blood samples from these mice confirmed the presence of Ty1 nanobodies (Figure 4(a)). Quantitative analysis of the blot densities confirmed that there was a significantly higher concentration of Ty1 Nb generated by EcN-Ty1 in the gut that was able to translocate and migrate to the systemic circulation (Figure 4(b)). We further evaluated the functional impact of this translocation

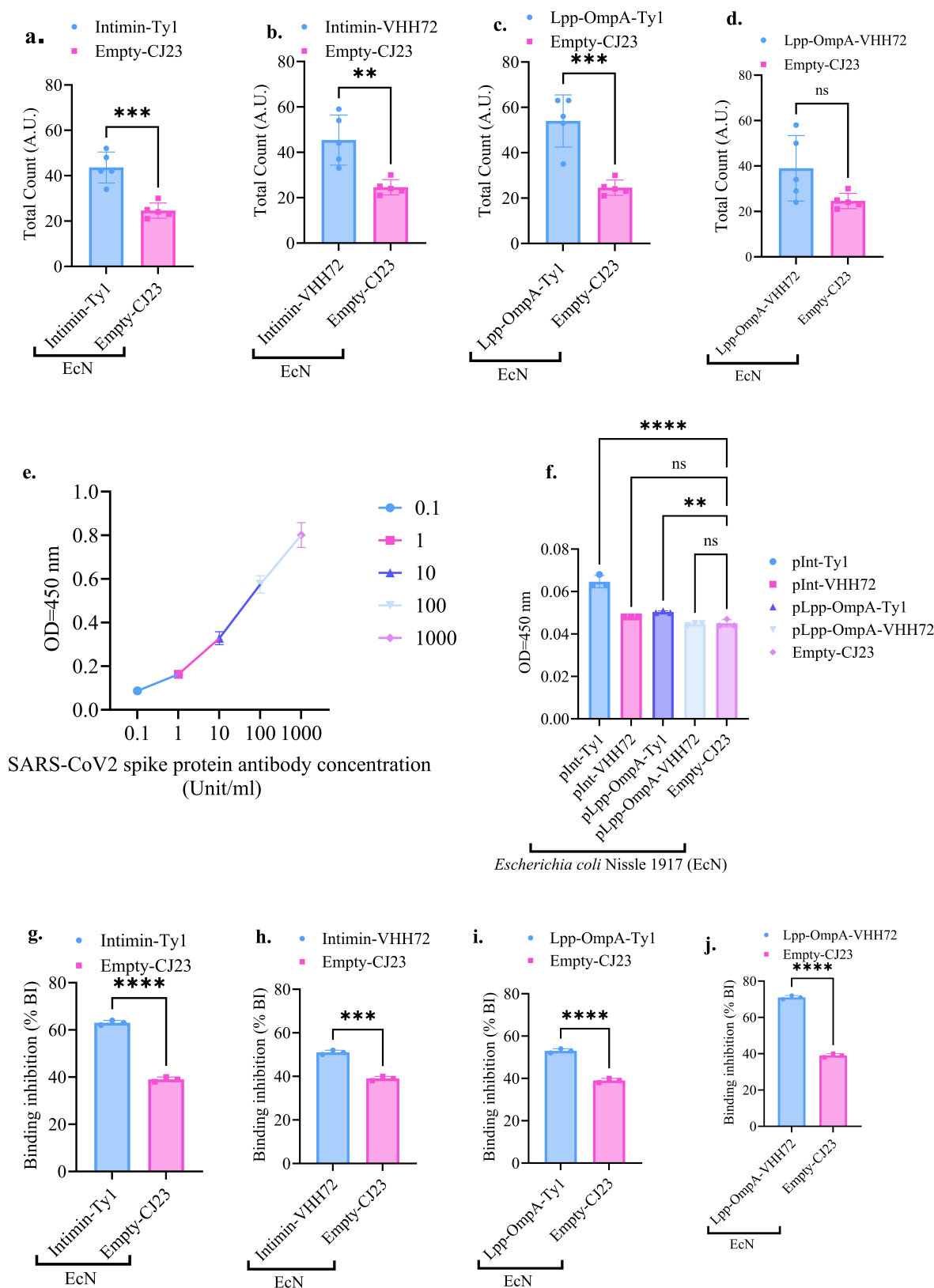


Figure 3. Anti-spike nanobody bearing bacteria inhibit spike-RBD and ACE2 receptor interaction. Functional expression of nanobodies was confirmed with a fluorescence-based assay (a-d). Spike-RBD-ACE2 receptor inhibition assay was performed using engineered bacteria. An indirect ELISA (e) standard plot to confirm the assay using engineered bacteria (f). Percent spike-RBD-ACE2 receptor binding inhibition assay using Ty1 nanobody-plnt-Ty1 (g), pLpp-OmpA-Ty1 (h), VHH72 nanobody- plnt-VHH72 (i), and pLpp-OmpA-VHH72 nanobody (j) compared to WT-*EcN*. Images were acquired using fluorescent microscope (Leica Microsystems) and analyzed with ImageJ's Fiji software. Absorbance was measured at 450nm using WT-*EcN* as a control. Graphs were plotted using GraphPad prism 8.0.v, significance was determined using paired t^2 -test, level of significance was set as ** $p < 0.05$; *** $p < 0.01$; **** $p < 0.001$, ns- not significant, (WT-*EcN*- wild-type *E. coli* nissle 1917).

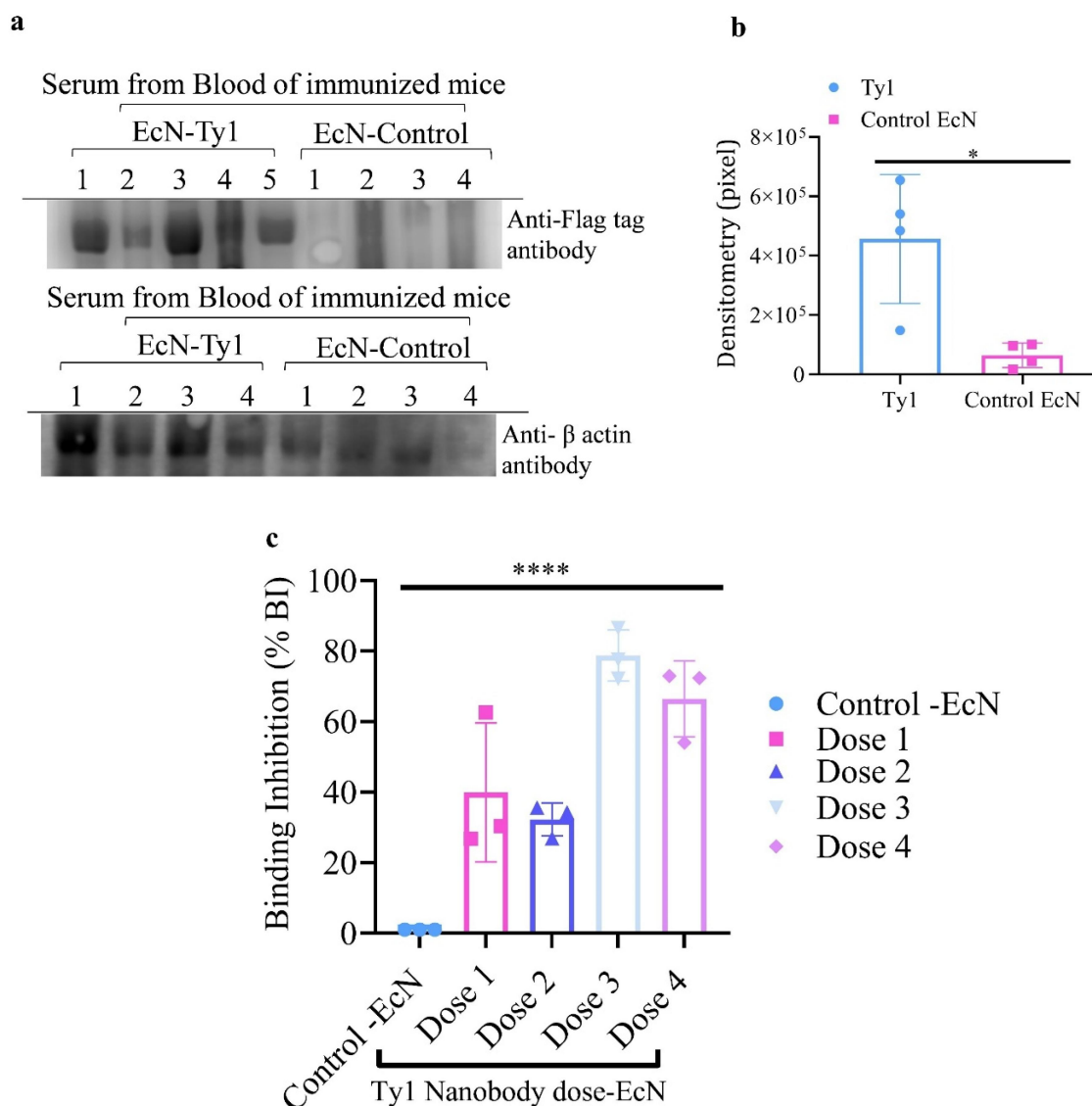


Figure 4. Detection of nanobodies and pseudovirus neutralization assay from serum of EcN-Ty1 treated mice. Western blot analysis (a-b) and pseudovirus neutralization assay (c) (luciferase) was performed using serum samples collected from the mice with EcN-Ty1 and control bacteria (EcN). Plates were read for luciferase expression at OD₄₅₀ using *EnVision* 2102 multilabel Reader (Perkin Elmer). Graphs were plotted using GraphPad prism 8.0.v, and significance was determined using paired t^2 -test, level of significance was set as $^{**}p < 0.05$; $^{***}p < 0.01$; $^{****}p < 0.001$, ns- not significant.

using a pseudovirus-ACE2 neutralization assay with serum samples. Our results demonstrated a notable inhibition of binding, showing approximately 40% inhibition post the initial dose. This inhibition slightly decreased to 38% after the second dose but then peaked at 75% following the third dose, before stabilizing at around 60% after the fourth dose (Figure 4(c)). These outcomes indicate that the therapeutic response progressively increases with repeated doses, but further studies are required to confirm long-term effects beyond the initial dosing period. The smaller size of

nanobodies, compared to conventional antibodies, likely facilitates their passage through the gut-blood barrier, allowing for their detection in the bloodstream.^{32,33} This suggests a promising avenue for the delivery of therapeutic agents via orally administered bacteria.

Comparison of EcN-Ty1 with monoclonal antibodies

Next, we compared the efficacy of Ty1 nanobody-expressing EcN (EcN-Ty1) administered orally to the standard of care, anti-spike monoclonal

antibodies (mAb), administered intravenously (i. v.). After five days, we collected serum, intestinal fluid, and bronchoalveolar lavage (BAL) fluid samples from the mice for pseudovirus neutralization assays. The results showed no significant difference in the inhibition of pseudovirus-ACE2 interaction between the serum of mice treated with mAb and those treated with EcN-Ty1 (Figure 5(a)), suggesting similar efficacy. However, the EcN-Ty1 treatment resulted in significantly higher inhibition in the intestinal fluid (~85%) (Figure 5(b)) and BAL samples (59.07%) (Figure 5(c)). Further analysis of IgG levels revealed no significant difference in serum (Figure 5(d)) and intestinal fluid

(Figure 5(e)) IgG concentrations between the two treatments. However, significantly lower IgG levels were observed in the BAL of the EcN-Ty1 group compared to the mAb group (Figure 5(f)). The IgG values were above baseline IgG levels in naïve mice (Supplementary Figure S6, Supplementary Table 4). These findings suggest that while both treatments are similarly effective in serum, EcN-Ty1 provides superior efficacy, particularly in the lungs and intestines, as indicated by higher inhibition of pseudovirus-ACE2 interaction. The significant inhibition of pseudovirus-ACE2 interaction in the intestines and lungs (BAL) of the EcN-Ty1 group, despite lower IgG levels in BAL, suggests

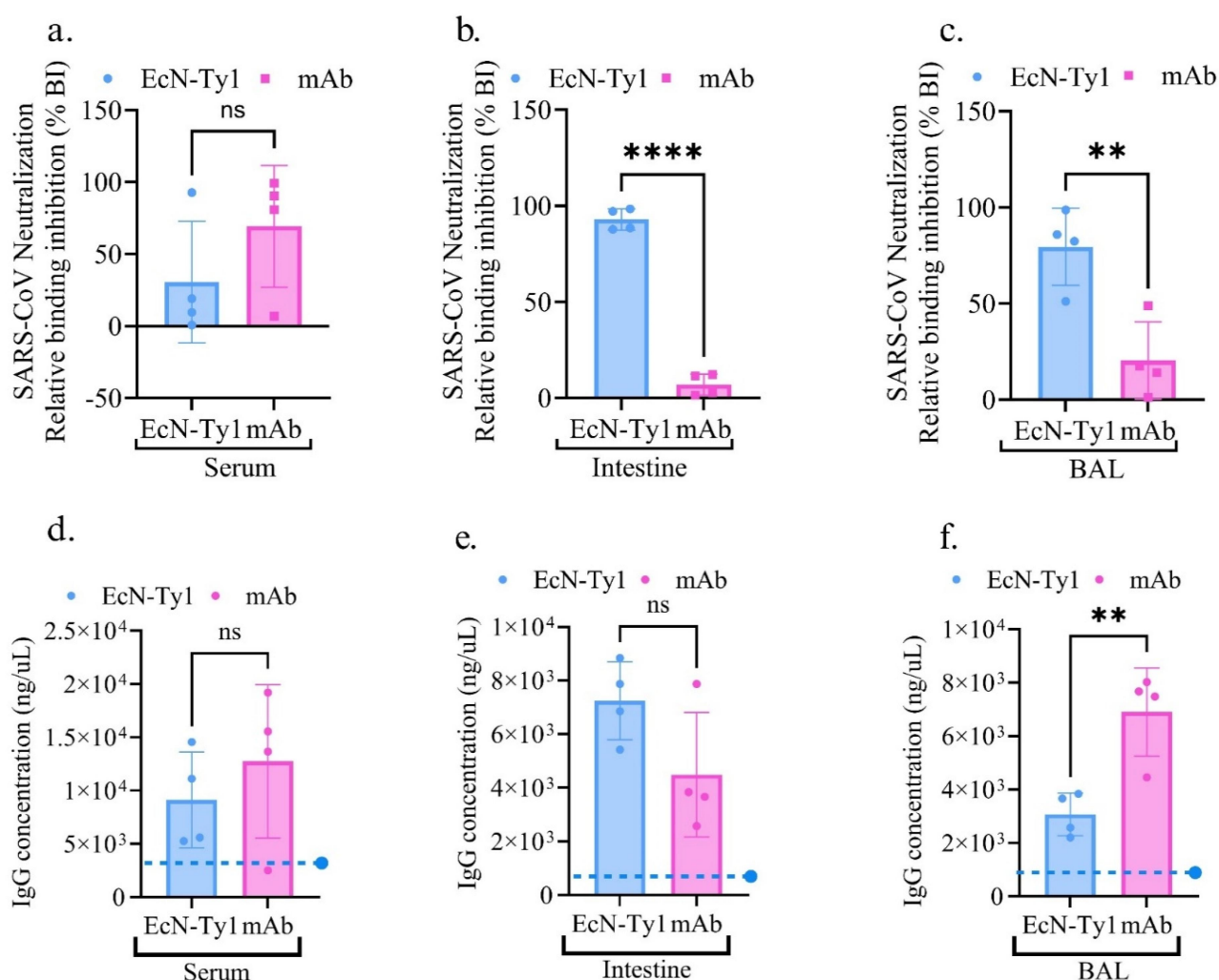


Figure 5. Pseudovirus neutralization assay using EcN-Ty1 and mAbs recovered from the serum, intestine and BAL with corresponding IgG levels. pseudovirus neutralization assay (luciferase) was performed using serum (a), intestine (b) and BAL (c). The IgG concentration quantified from serum (d), intestine (e) and BAL (f). Samples collected 5 days, after oral administration of Nb and i. V. administration of mAb, respectively. Neutralization assay plates were read for luciferase expression at OD₄₅₀, and IgG ELISA was read at 340nm using *varioskan lux* multimode plate reader (thermo fisher scientific). Dotted blue lines represent standard IgG levels in a 20–25g, C57BL6 mice. Graphs were plotted using GraphPad prism 8.0.v, and significance was determined using paired t^2 -test, level of significance was set as “*” $p < 0.05$; “***” $p < 0.01$; “****” $p < 0.0001$, ns- not significant. Schematics were drawn using Biorender.

a substantial contribution from nanobodies in neutralization. Nanobodies are smaller and can penetrate tissues and barriers, such as the gut-blood and blood-brain barriers more easily, potentially reaching more effectively in mucosal surfaces. The presence of active nanobodies at these sites may compensate for or even exceed the neutralization capacity typically attributed to IgG antibodies.

Surface anchored spike-glycoprotein nanobodies were detected on secreted outer membrane vesicles (OMVs)

To understand how nanobodies traverse the gut-blood and blood-brain barrier, we focused on the role of bacterial outer membrane vesicles (OMVs) in their transport. OMVs, particularly from Gram-negative bacteria, are increasingly recognized for their potential in delivering vaccines and therapeutic agents, offering advantages over live attenuated vaccines.^{22,34} OMVs are naturally produced through outer membrane blebbing and can distribute therapeutic agents within the intestinal lumen, reaching dendritic cells (DCs) and potentially entering the systemic circulation (Figure 6(a)).^{35–37} Our studies suggest that our engineered constructs are likely to release OMVs containing Ty1 and VHH72 nanobodies, tethered to Intimin and Lpp-OmpA. We isolated and quantified these OMVs using the bicinchoninic acid assay (BCA). The yields obtained were: WT-*EcN* OMVs (1.587 ± 0.5 mg/mL), pInt-Ty1 (5.602 ± 0.5 mg/mL), Int-VHH72 (4.219 ± 0.5 mg/mL), pLpp-OmpA-Ty1 (3.064 ± 0.5 mg/mL), and pLpp-OmpA-VHH72 (1.181 ± 0.5 mg/mL). Transmission electron microscopy (TEM) analysis of these OMVs revealed their nanoscale size, ranging from approximately 75 to 400 nm in diameter during OMV formation stage (Figure 6(c)) and separated OMVs (Figure 6(c)). We also analyzed their size distribution using dynamic light scattering (DLS) (Figure 6(d) and Supplementary Figure S7). The mean vesicle diameter for Intimin-anchored nanobodies was slightly larger (90 ± 10 nm) than OMVs of WT-*EcN* (80 ± 5.0 nm) (Figure 6(e–f)). However, the mean vesicle diameter for Lpp-OmpA-anchored nanobodies was significantly smaller (60 ± 7.5 nm) than OMVs carrying Intimin-anchored nanobodies and WT-*EcN* (Figure 6(g–h)). All exhibited a relatively uniform size distribution

(0.2–0.3) as indicated by their polydispersity index (PDI) values.³⁸ Further, we confirmed the presence of surface-anchored nanobodies on these OMVs. SDS-PAGE and Western immunoanalysis with an HRP-conjugated anti-flag tag antibody showed distinct bands at ~89.4 kDa and 90.5 kDa, corresponding to pInt-Ty1 and pInt-VHH72 nanobodies, respectively, and similarly for pLpp-OmpA-Ty1 and pLpp-OmpA-VHH72, by bands at ~32.6 kDa and 33.8 kDa, respectively, contrasting with the absence of such bands in OMVs from WT-*EcN* (Figure 6(i–j)). This evidence supports the conclusion that engineered *EcN* can effectively display nanobodies on OMVs for potential systemic delivery.

OMVs bearing anti-spike nanobodies inhibit pseudovirus and ACE2 interaction

We aimed to assess if nanobodies on OMVs could block the interaction between pseudoviruses and ACE2 receptors. We used OMVs derived from both control *EcN* and *EcN* expressing anti-Spike nanobodies, Ty1 and VHH72, in a pseudovirus-ACE2 neutralization assay. The assay was performed with three different OMV concentrations: 22 µg/mL, 3 µg/mL, and 0.3 µg/mL. At the highest concentration (22 µg/mL), OMVs with the Intimin-Ty1 nanobody showed the most significant inhibition of the pseudovirus-ACE2 receptor interaction, approximately 30–32%. This was notably higher than the inhibition observed with Lpp-OmpA-Ty1 OMVs, which was around 15–18% (Figure 7(a)). At a lower concentration of 3 µg/mL, pInt-Ty1 OMVs again demonstrated superior inhibition, in the range of 31–34%, compared to Lpp-OmpA-Ty1 OMVs (15–18%) (Figure 7(b)). However, at the lowest concentration tested (0.3 µg/mL), only the pInt-Ty1 OMVs showed a modest inhibition effect of 3–4%, with Lpp-OmpA-Ty1 OMVs showing no significant inhibition (Figure 7(c)). For the VHH72 nanobody constructs, pInt-VHH72 OMVs exhibited greater pseudovirus-ACE2 receptor inhibition than pLpp-OmpA-VHH72 OMVs at 22 µg/mL (15–16% vs. 10–11%) (Figure 7(d)). This difference was more pronounced at 3 µg/mL, with pInt-VHH72 achieving 30–35% inhibition compared to only 10% for pLpp-OmpA-VHH72 (Figure 7(e)). At the lowest concentration of 0.3 µg/mL, neither pInt-VHH72 nor pLpp-OmpA-VHH72 OMVs showed

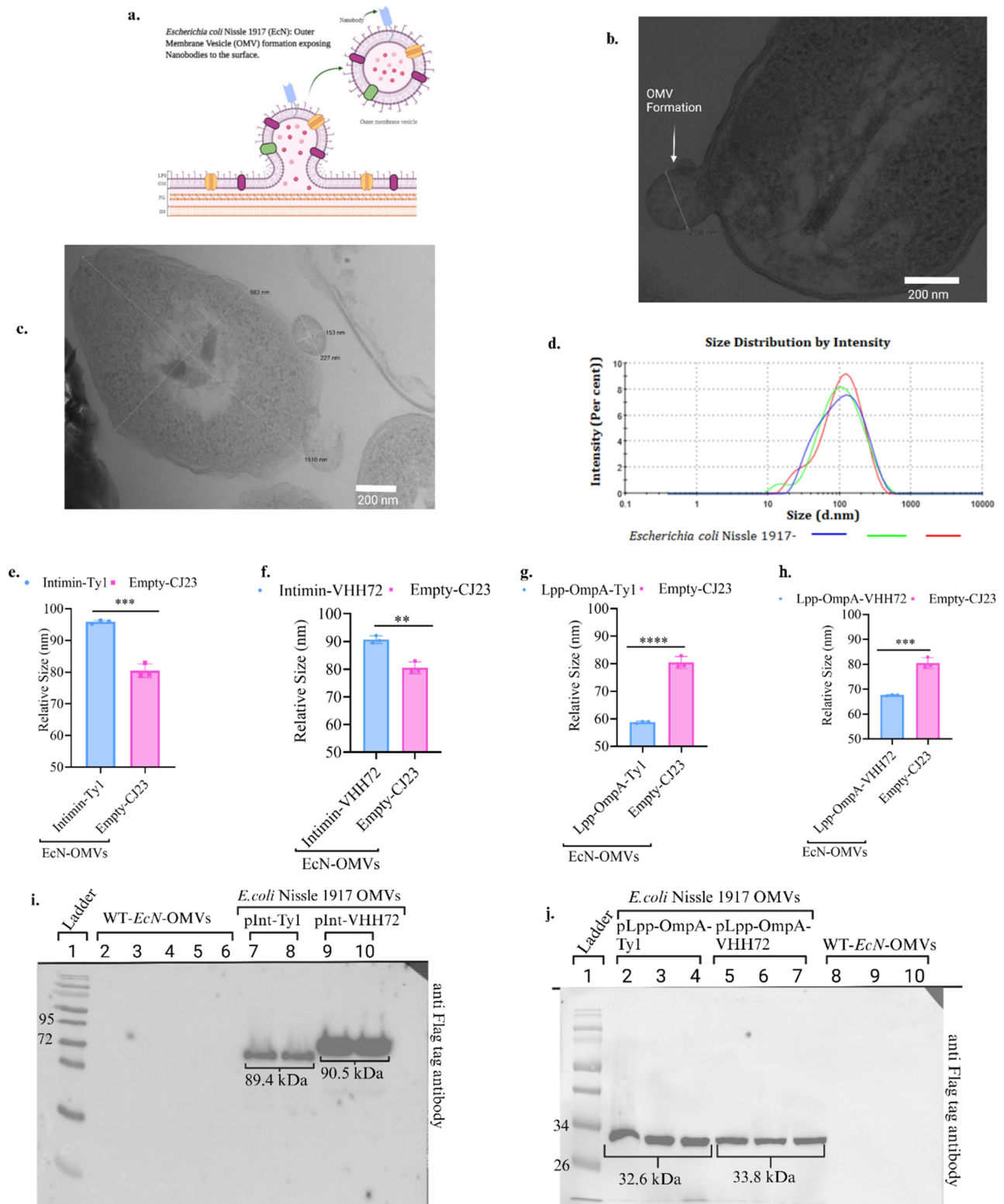


Figure 6. Nanobody expression on OMVs. Schematic of OMV formation in *E. coli* nissle 1917 (a). OMVs were analyzed via transmission electron microscopy (TEM) showing OMV formation and (b) separated OMVs (c) and dynamic light scattering (DLS), (d) using Zetasizer (Malvern). OMV size comparison of OMVs collected from pInt-Ty1 (e), pInt-VHH72 (f), pLpp-OmpA-Ty1 (g), and pLpp-OmpA-VHH72 (h) with OMVs collected from WT-EcN. Confirmation of nanobodies on OMVs was performed with SDS-PAGE and Western blot analysis using anti-flag tag antibody (Invitrogen). OMVs collected from pInt-Ty1 and pInt-VHH72 (i). Lane 1 was loaded with ladder followed by lane 2–6 with WT-EcN OMVs, 7–8 with pInt-Ty1 and 9–10 with pInt-VHH72. Lpp-OmpA attached nanobodies were also run on SDS-PAGE gels (j) and loaded as- lane 1 with ladder, lanes 2–4 with pLpp-OmpA-Ty1, followed by lane 5–7 with pLpp-OmpA VHH72 and lane 8–10 with WT-EcN-OMVs. We used protein ladder (EZ-Run™ pre-stained rec protein ladder). Blots were developed using the ChemiDoc™ imaging system (BioRad), while graphs were plotted using graph pad prism 8.0.v, significance was determined using paired t^2 -test, level of significance was set as “*” $p < 0.05$; “***” $p < 0.01$; “****” $p < 0.001$, ns- not significant. Schematics were drawn using Biorender.

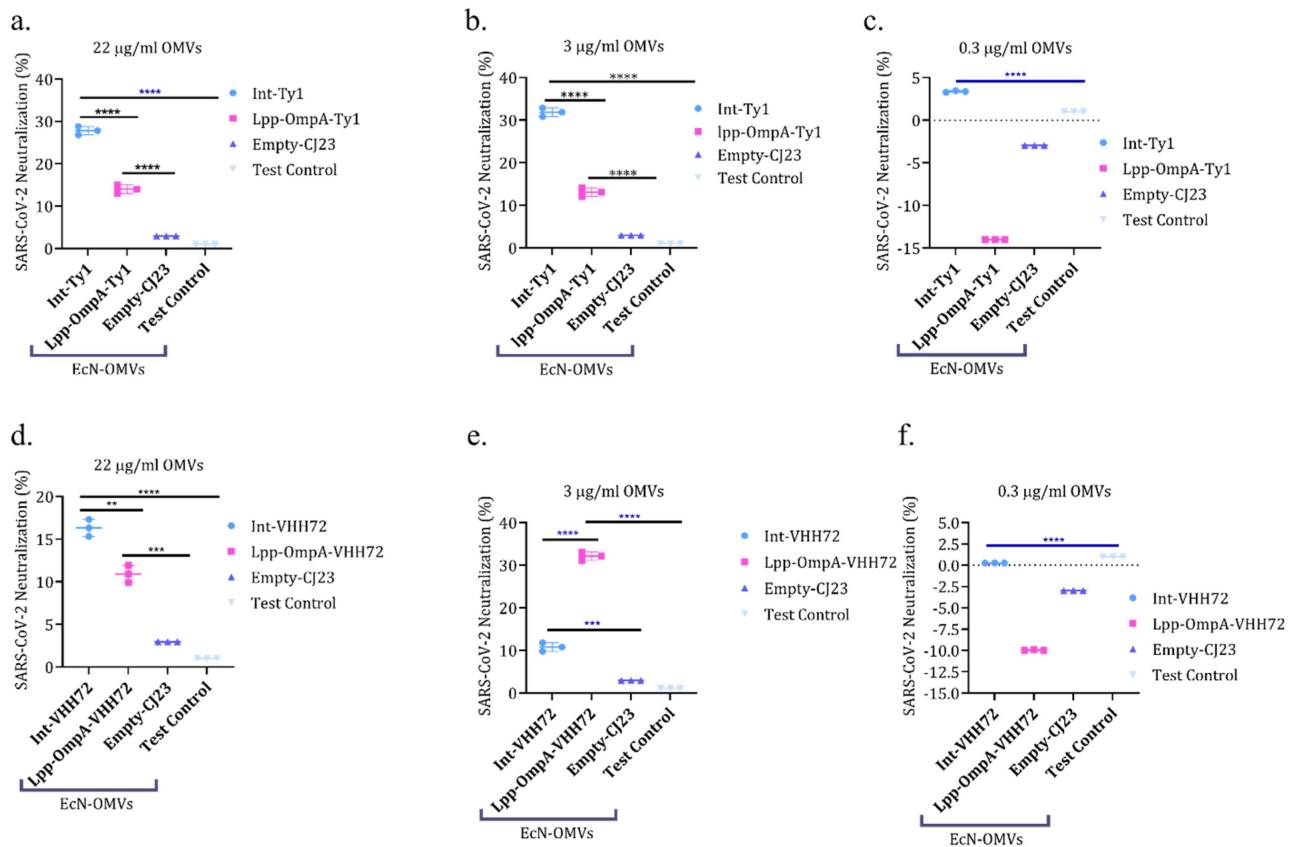


Figure 7. Anti-SARS-CoV-2 nanobody bearing OMVs inhibit pseudoviruses expressing spike protein from binding with ACE2 receptor. Different concentrations of OMVs collected from plnt-Ty1 and lpp-OmpA-Ty1 (a, b, c), and plnt-VHH72 and lpp-OmpA-VHH72 (d, e, f) along with OMVs of control WT-*EcN* were used in COVID-19 pseudovirus neutralizing antibody assay (luciferase) (Abnova). Plates were read for luciferase expression using *EnVision* 2102 multilabel Reader (Perkin Elmer) and graphs were plotted using GraphPad prism 8.0v, significance was determined using paired t^2 -test, level of significance was set as “*” $p < 0.05$; “**” $p < 0.01$; “***” $p < 0.001$, ns- not significant.

significant inhibition (Figure 7(f)). These results indicate that Intimin is a more effective anchor for nanobodies on OMVs in terms of facilitating the neutralization of pseudovirus interaction with the ACE2 receptor, compared to Lpp-OmpA-based anchors. Moreover, the Ty1 nanobody constructs were effective in inhibiting the pseudovirus-ACE2 interaction even at the lowest concentration tested, whereas the VHH72 nanobody constructs showed significantly reduced effectiveness below 3 µg/mL.

Translocation of nanobodies to distal organs via OMV-mediated transport

We hypothesized that nanobodies expressed on OMVs might be capable of reaching organs beyond the gut, particularly the lungs and brain, which are known targets of SARS-CoV-2 infection.³⁹ To investigate this, we orally administered pInt-Ty1-

expressing bacteria to one group of mice and control bacteria to another, daily for four days. Subsequent immunofluorescence analysis of the harvested lungs and brains, using anti-flag tag antibodies, was conducted to detect the presence of nanobodies. Our findings revealed a distinct fluorescence signal in the lungs of mice treated with pInt-Ty1-expressing bacteria (Figure 8(a)), contrasting with the absence of such signals in the lungs of control mice (Figure 8(b)). This difference was statistically significant (Figure 8(c)). More intriguingly, the brains of mice treated with pInt-Ty1-expressing bacteria also showed the presence of nanobodies (Figure 8(d)), whereas the brains of control mice did not (Figure 8(e)), again with a notable difference between the two groups (Figure 8(f)). These observations suggest that OMVs may play a crucial role in transporting nanobodies from bacteria across the gut-blood

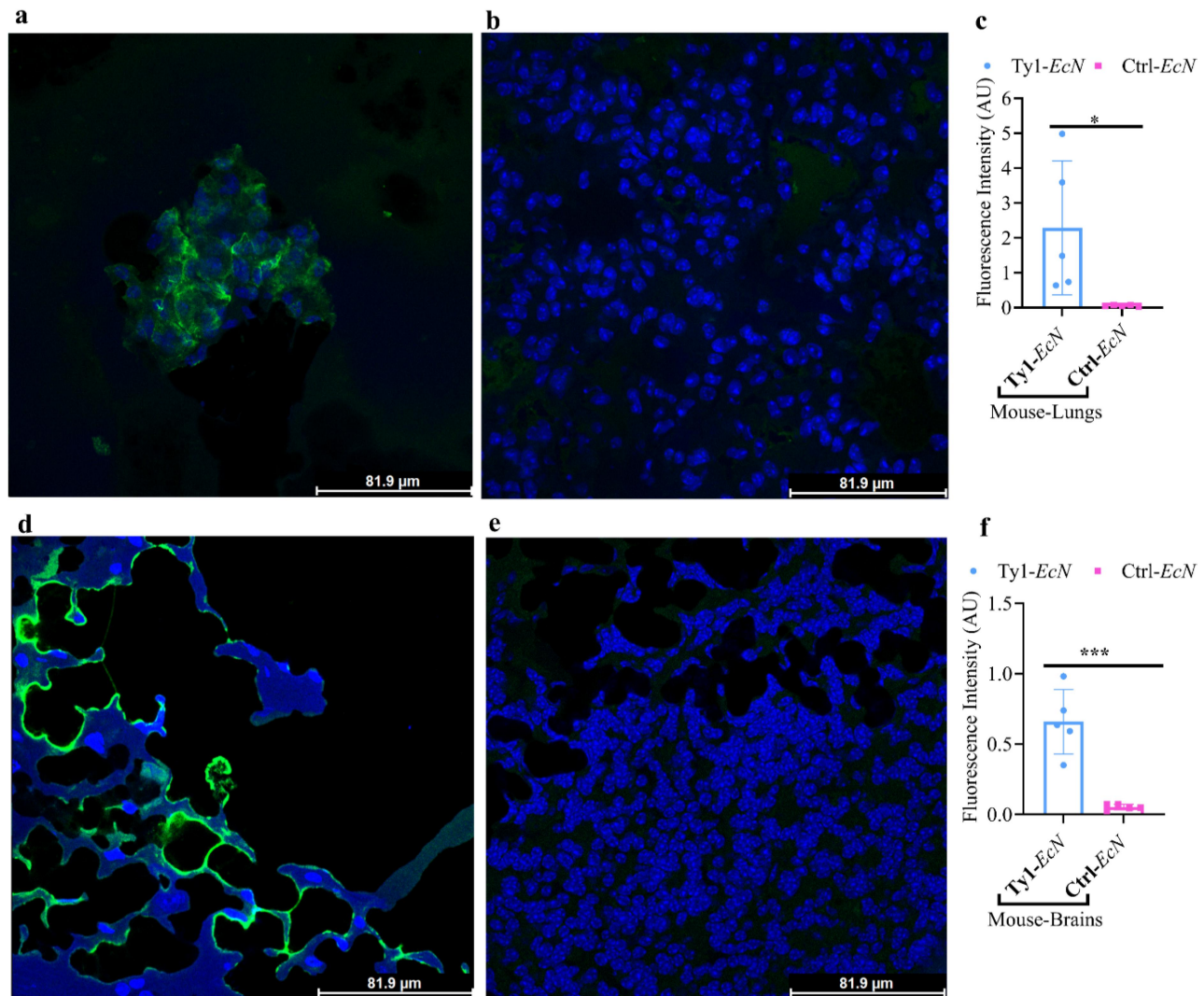


Figure 8. OMVs were detected in brain and lungs of immunized animals. Ty1 bearing and control bacteria were orally administered in two different groups of mice and their organs were harvested. Organs were subjected to OCT-embedded immunohistochemistry, stained with anti-flag tag antibody and images were taken using Confocal microscopy. Lungs harvested from Ty1 (a) and control bacteria (b). Images were quantified using ImageJ Fiji (c). Brains harvested from Ty1 (d) and control bacteria (e) were quantified using ImageJ Fiji and plotted using graph pad prism 8.0v. Significance was determined using paired t^2 -test, level of significance was set as “*” $p < 0.05$; “**” $p < 0.01$; “****” $p < 0.001$, ns- not significant.

barrier into the systemic circulation, and then further across the blood-lung and blood-brain barriers into the lungs and brain, respectively. This implies a promising potential for OMVs in delivering nanobody-based therapeutics to distal organs affected by SARS-CoV-2.

Surface expression of spike protein on EcN

In our second approach, we focused on creating active immunity by engineering EcN to express the SARS-CoV-2 spike protein on its surface. We utilized Intimin to anchor the spike protein onto

the bacterial surface (Figure 9(a) and Supplementary Figure S8).²⁶ The successful expression of the intimin-spike fusion protein was confirmed through SDS-PAGE Western blot analysis, which revealed a distinct ~106.4kDa band matching the expected size of Intimin-spike. In contrast, no bands were detected in EcN cells carrying the pSF-empty plasmid, affirming the specific expression of the spike protein on EcN (Figure 9(b)). We then assessed if EcN cells expressing the spike protein would interact with those bearing nanobodies. This was hypothesized to potentially lead to

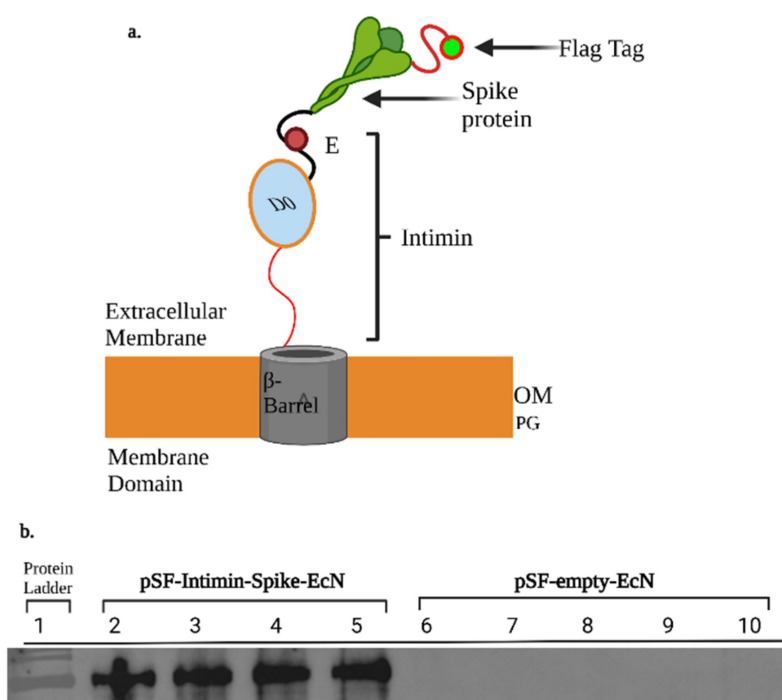


Figure 9. Confirmation of expression of spike protein with SDS-PAGE analysis. Schematic design of spike protein surface displayed using Intimin anchor (a). Confirmation of the spike-RBD expression with SDS-PAGE Western blot analysis, showing ~106.4kDa bands in pSF-Intimin-spike loaded wells and absence of any bands in pSF-empty-EcN loaded wells. Blots were developed using anti-flag tag antibody, and the ChemiDoc™ imaging system (BioRad). Schematics were drawn using Biorender.

bacterial aggregation and precipitation (Supplementary Figure S9, a).^{40,41} Indeed, when nanobody-bearing EcN was incubated with spike-bearing EcN, significant bacterial aggregation occurred, evidenced by a marked reduction in optical cell density (OD_{600}).⁴⁰ Notably, EcN expressing pInt-Ty1, Lpp-OmpA-Ty1, and pInt-VHH72 nanobodies showed considerable aggregation with spike-bearing EcN, in descending order of effectiveness: pInt-Ty1, Lpp-OmpA-Ty1, and then pInt-VHH72 (Figure S9, b-e). However, EcN with Lpp-OmpA-VHH72 nanobodies did not demonstrate a notable difference in aggregation compared to the wild-type EcN (Supplementary Figure S9, e). These findings confirm not only the successful surface expression of functional spike protein on EcN but also its ability to bind to corresponding nanobodies. Furthermore, the results underscore the superiority of Intimin over Lpp-OmpA as an anchoring protein for the expression of both nanobodies and spike proteins on the bacterial surface.

Oral administration of EcN-spike in mice induces an anti-spike immune response

We investigated whether oral administration of EcN-spike would induce an immune response and generate anti-spike antibodies. We first examined bacterial residence time in the mouse gut using qPCR analysis of fecal samples ($n = 4$). We found that EcN has a typical residence time of ~10–12 days in the gut after a single oral administration and about at least another 30 days after second dose on day 25, with the $1/Ct$ peaking around the 30th day (Figure 10(a)). This indicates the capability of EcN-spike in delivering recombinant spike protein for a prolonged period when administered orally. To further confirm gut colonization, we used EcN-spike and wild-type (WT) EcN expressing a luciferase reporter, enabling us to visualize the bacteria in the gut through bioluminescence imaging (BLI) over four weeks (Supplementary Figure S10). We tested three oral administration regimens of EcN-spike in mice to evaluate antibody response: a single dose, two doses bi-weekly, and

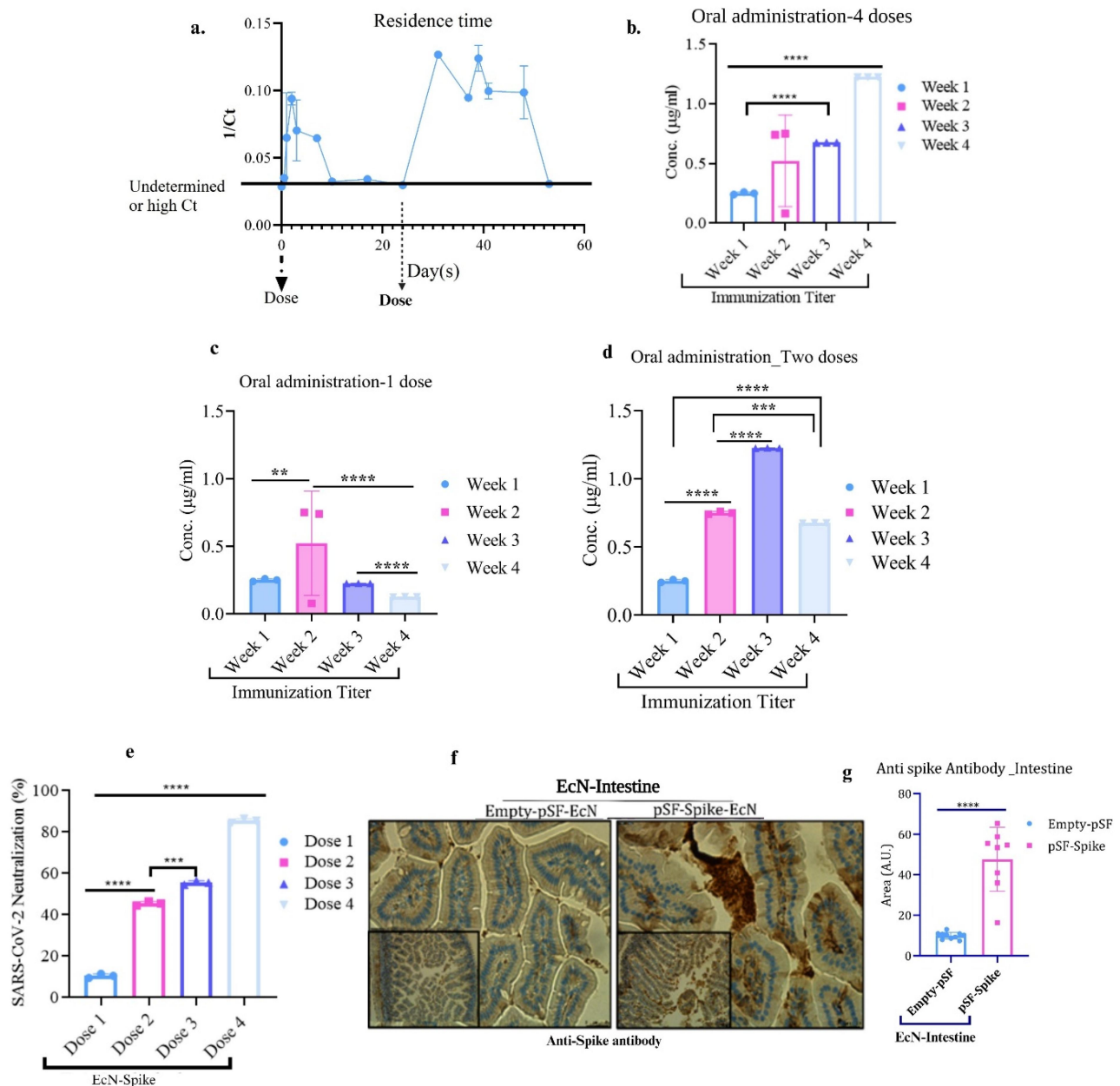


Figure 10. *EcN*-spike induces host immune response and inhibits pseudoviruses expressing spike from interacting with ACE2 receptor. Bacterial residence time was calculated using qPCR (a), mouse anti-SARS-CoV-2 antibody IgG titer serologic assay was performed using serum samples collected from the mice orally administered with *EcN*-spike with four doses one week apart (b), one dose was given and blood was collected for 4 weeks, one week apart (c) and two doses biweekly and blood was drawn each week for 4 weeks (supplemental data: Fig S10) (d). Y-axes represent anti-spike antibody concentration generated in response to spike protein expressing bacteria in the mouse gut. Mice orally administered with 4 doses of bacteria one week apart for 4 weeks was used for serum collections and used in COVID-19 pseudovirus neutralizing antibody assay (luciferase) (e). Plates were read for luciferase expression at OD₄₅₀ using *EnVision* 2102 multilabel Reader (Perkin Elmer) and graphs were plotted using GraphPad prism 8.0.v, significance was determined using one way ANOVA for multiple comparison. IHC analysis on mouse intestines (f), quantified with ImageJ analysis (g). Level of significance was set as “*” $p < 0.05$; “**” $p < 0.01$; “***” $p < 0.001$, ns- not significant. Schematics were drawn using Biorender.

four weekly doses. The continuous four-week dose regimen in naive C57BL6/J mice showed a steady increase in antibody levels, rising from approximately 0.25 µg/mL after the first dose to 1.25 µg/mL after the fourth dose (Figure 10(b)). For the

single dose regimen, serum analysis indicated anti-spike antibody titers of about 0.2 µg/mL after the first week, peaking at roughly 0.8 µg/mL in the second week before gradually decreasing (Figure 10(c)). The bi-weekly two-dose regimen

resulted in a gradual increase in antibody titers, reaching a peak at week three ($\sim 1.25\mu\text{g/mL}$) and then diminishing (Figure 10(d)). Further, we assessed if the antibodies generated could inhibit the interaction between COVID pseudoviruses and the ACE2 receptor. Serum samples from mice given EcN-spike and control EcN were tested in a Pseudovirus neutralization assay (Supplementary Figure S11). We noted a significant correlation between antibody titers and the percentage of pseudovirus neutralization, with neutralization increasing with each additional dose of spike-expressing EcN. Serum from the first week showed around 10% neutralization, increasing to about 45% after the second dose, 55% after the third, and peaking at around 80% after the fourth dose (Figure 10(e)). Schematics of animal immunizations and serum collection timepoints are shown in Supplementary Figure S12. While BLI and qPCR analyses indicated a decrease in gut bacterial population over time, we conducted immunohistochemistry (IHC) analysis for spike protein after four weeks of the two-dose regimen to verify if EcN-spike persisted in the gut. We found three times higher spike protein levels in mice treated with EcN-spike compared to those with EcN alone (Figure 10(f-g)), suggesting significant ongoing presence and stable expression of spike protein by the engineered bacteria in the gut.

Comparison of EcN-spike with mRNA vaccine

Next, we compared the efficacy of EcN-Spike to the standard mRNA vaccine (Moderna COVID-19 vaccine Spikevax™) in eliciting an immune response in mice. EcN-Spike was administered orally, while the mRNA vaccine was given intramuscularly. Five days post-administration, we collected serum, intestinal fluid, and bronchoalveolar lavage (BAL) fluid samples for a pseudovirus neutralization assay. The results showed that mice vaccinated with the mRNA vaccine had significantly greater inhibition of pseudovirus-ACE2 interaction compared to those receiving EcN-Spike. Specifically, the vaccinated mice exhibited a ~ 3.45 -fold increase in serum inhibition (Figure 11(a) and a ~ 2.6 -fold increase in intestinal fluid inhibition (Figure 11(b)), and Supplementary Figure S13).

However, there was no significant difference in inhibition between the two groups in the BAL of vaccinated mice (Figure 11(c)). Further analysis of IgG levels revealed the vaccinated group displayed significantly higher IgG levels in the serum (Figure 11(d)), suggesting a positive correlation between pseudovirus inhibition and IgG levels. However, the IgG levels in the intestine were significantly higher in the EcN-spike group compared to vaccine group (Figure 11(e)), but not significantly different in the BAL (Figure 11(f)). For reference, the standard IgG levels are marked in the graphs (Figure 11(d-f)) and detailed in the Supplementary Table 5. These findings suggest that while the mRNA vaccine effectively induced a stronger systemic immune response, EcN-spike may promote a strong localized immune response in the gut and lungs. The differential IgG levels and neutralization efficacy across different compartments suggest distinct immune response profiles between the EcN-Spike and mRNA vaccine treatments.

EcN-spike induces mucosal immunity

Previous studies have indicated that the SARS-CoV-2 virus initially enters the body through the mouth mucosa, triggering a robust immune response marked by the activation of various immune cells and molecules, including IgA.⁴² This response then spreads throughout the mucosal system. In light of this, our objective was to determine if oral administration of EcN expressing the Spike protein could stimulate mucosal immunity in mice. To investigate this, we administered EcN-Spike and control-Empty-pSF-EcN bacteria orally to mice for four weeks. Post-administration, we analyzed serum and intestinal samples from the animals. Our findings showed a notable increase in IgA levels in the serum of mice treated with the Spike protein-expressing bacteria compared to those given the control bacteria (Figure 12). This result is significant, as IgA is known to play a crucial role in defending against various pathogens. It achieves this through mechanisms such as neutralization, prevention of pathogen adherence, and agglutination.⁴² Given that IgA has been reported to remain effective for at least three months, our

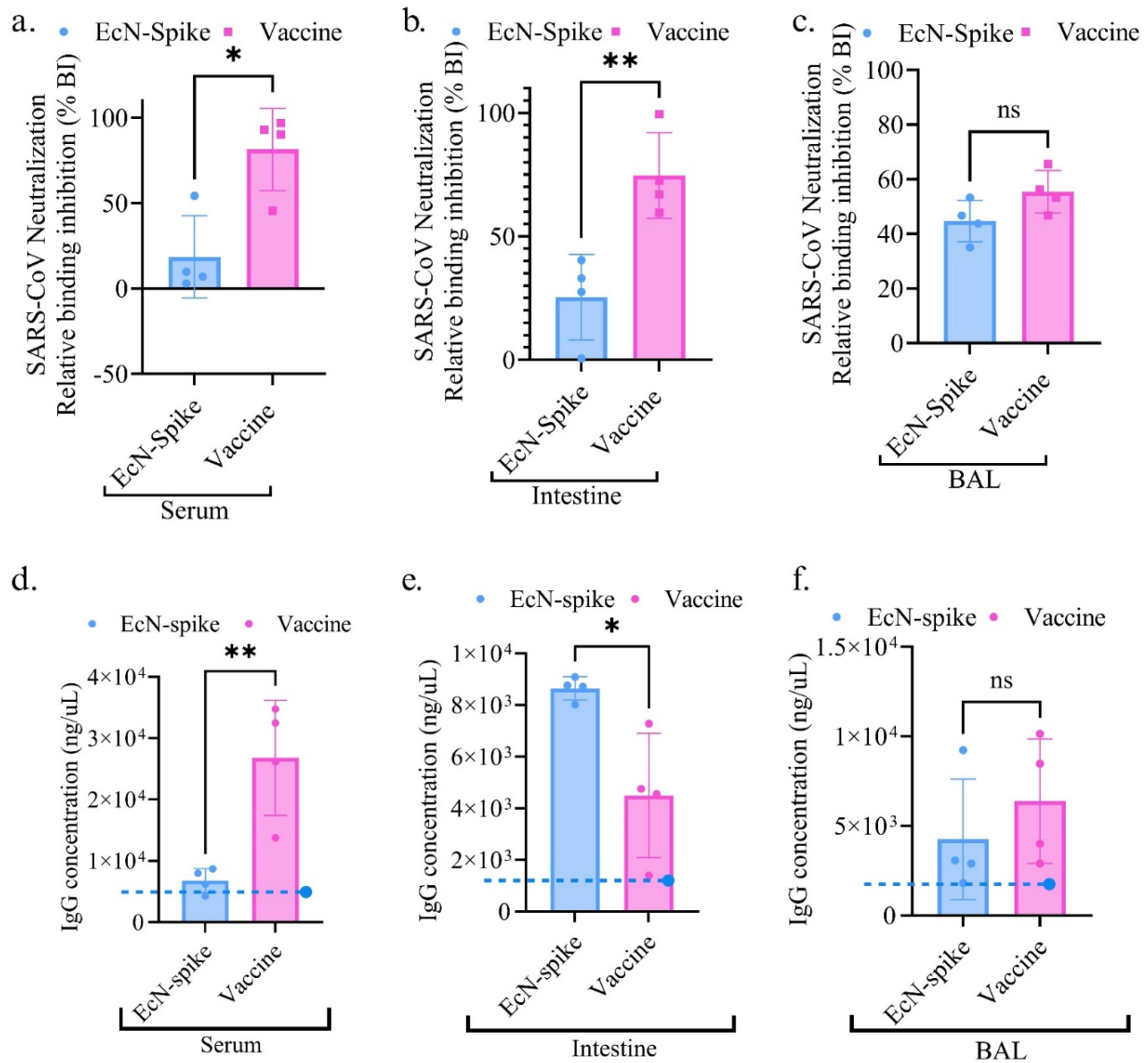


Figure 11. Comparison of pseudovirus neutralization inhibition with EcN-spike and mRNA vaccinated animals using serum, intestine and BAL with corresponding IgG levels. Pseudovirus neutralization assay (luciferase) was performed using serum (a), intestine (b) and BAL (b). IgG concentration quantified using ELISA in serum (d), intestine (e) and BAL (F). Samples collected 5 days after oral administration of EcN-spike and i.M. administration of mRNA vaccine, respectively. Neutralization assay plates were read for luciferase expression at OD₄₅₀ and IgG ELISA at 340 nm using *varioskan lux* multimode plate reader (thermo fisher scientific). Dotted blue lines represent standard IgG levels in a 20–25 g, C57BL6 mice. Graphs were plotted using GraphPad prism 8.0.v, and significance was determined using paired t^2 -test, level of significance was set as “*” $p < 0.05$; “**” $p < 0.01$; ns- not significant. Schematics were drawn using Biorender.

findings suggest that it could offer substantial protection against SARS-CoV-2 infection.

In addition to serum analysis, we also analyzed the intestines from the test animals. Through immunohistochemistry (IHC) analysis, we aimed to detect the presence and levels of lymphoid T cells and myeloid cells. Our results revealed a significant increase in CD4⁺ and CD8⁺ T-cells,

as well as activated monocytes (CD11b), in the mice that received oral administration of EcN-Spike, in comparison to those that were given the empty-CJ23-EcN control. These findings are visually represented in Figure 13,(a-f). Furthermore, we noted a substantial rise in the levels of the pro-inflammatory cytokine IL1 β in the intestines of mice that were administered the

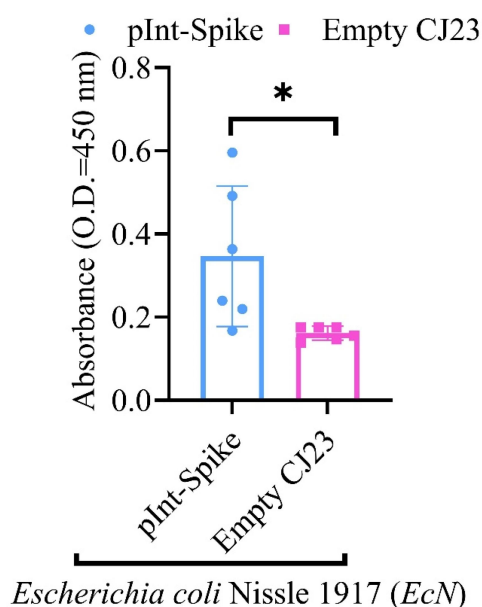


Figure 12. ELISA for IgA. Serum samples from mice orally administered with spike expressing and control bacteria (empty-pSF) were analyzed using an indirect ELISA (RayBiotech). Absorbance was read at 450 nm using varioskans lux (thermo fisher) plate reader and plotted using graph pad prism 8.0.V, significance was determined using paired t^2 -test, level of significance was set as “*” $p < 0.05$; “**” $p < 0.01$; “***” $p < 0.001$, ns- not significant.

Spike-expressing bacteria. This was in stark contrast to the levels observed in mice given the control bacteria, as shown in Figure 13(g-h). These outcomes indicate that EcN-Spike effectively enhances mucosal immunity within the gut. It achieves this by not only activating T cells and monocytes but also by stimulating the release of pro-inflammatory cytokines.

Comparison of EcN-spike with mRNA vaccine and EcN-Ty1 nanobody with monoclonal antibody treatment

To evaluate the effectiveness of our constructs compared to standard-of-care treatments, we conducted a study with four groups of animals: one group received oral administration of EcN-Spike, another received intramuscular administration of the mRNA vaccine, a third received oral administration of EcN-Ty1 nanobody, and the last group received intravenous administration of monoclonal antibodies (mAb). Five days after administration, samples were collected from serum, intestine, bronchoalveolar lavage (BAL) fluid, and feces for IgA analysis using ELISA. The results showed that

serum IgA levels were significantly higher in the EcN-Spike group compared to the mRNA vaccine group (Figure 14(a)). However, no significant differences in IgA levels were observed in the intestine, BAL fluid, or feces between these groups (Figure 14(b-d)). Similarly, no significant differences in IgA levels were detected between the EcN-Ty1 and mAb groups across all tested compartments: serum, intestine, BAL fluid, and feces (Figure 14(e-h)). IgA levels in both treatment groups (EcN-Spike and EcN-Ty1) were higher than in naïve mice (Supplementary Figure S14, Supplementary Table 5). The significantly elevated serum IgA levels observed in the EcN-Spike group compared to the mRNA vaccine group suggest that oral administration of EcN-Spike may more effectively stimulate systemic IgA production. This enhanced systemic IgA response could be attributed to the interaction between the engineered probiotic and gut-associated lymphoid tissue (GALT), which plays a central role in mucosal immune activation. The ability of EcN-Spike to interact with GALT likely facilitates IgA secretion into the bloodstream, offering potential systemic protection. Interestingly, the absence of significant differences in IgA levels across the intestine, BAL fluid, and feces among the groups suggests that mucosal IgA production was uniformly distributed regardless of the treatment type. The lack of differences between the EcN-Ty1 and mAb groups across all tested compartments indicates that both the nanobody-based and monoclonal antibody treatments achieve similar systemic and mucosal immune responses in this short-term evaluation.

Longitudinal evaluation of systemic and mucosal IgA responses induced by EcN-spike and mRNA vaccine

To evaluate the longitudinal systemic and mucosal immunogenicity of EcN-Spike, as an oral vaccine, we measured IgA concentrations in serum, intestinal fluid, BALF, and feces over a four-month period (Supplementary Figure S15). These responses were compared to those induced by the intramuscularly administered Moderna mRNA vaccine.

In the first month (4 weeks), EcN-Spike-treated mice exhibited higher serum IgA levels (mean $1280.9 \pm 111.4 \text{ ng}/\mu\text{L}$) compared to the vaccine group (mean $705.6 \pm 243.1 \text{ ng}/\mu\text{L}$), suggesting a robust early IgA response induced by EcN-Spike

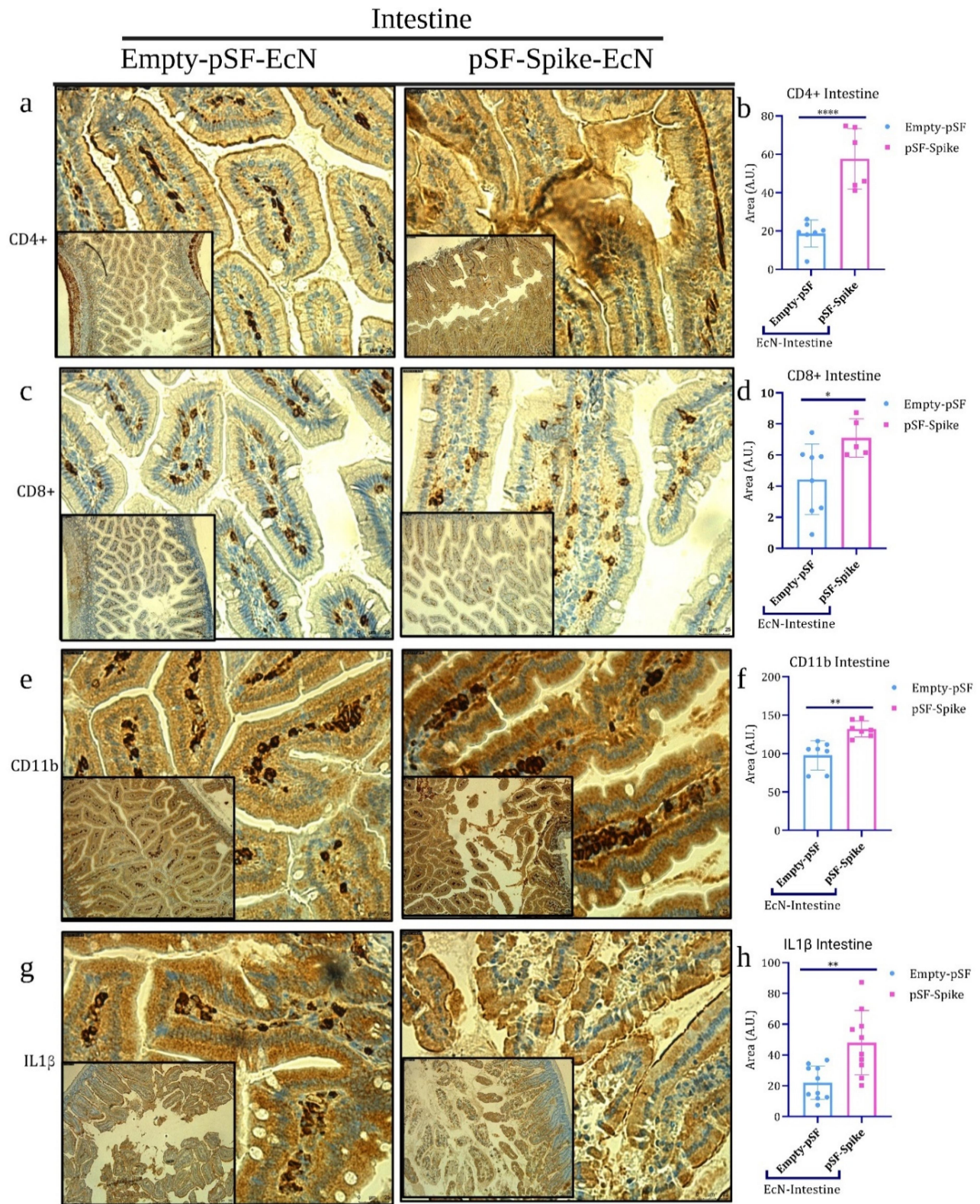


Figure 13. Immunohistochemical analysis of mouse intestines. Intestines harvested from the gut of mice orally administered with spike expressing and control bacteria were analyzed with IHC for CD4⁺ (a-b), CD8⁺ (c-d), CD11b (e-f), and IL1β (g-h) markers. Images were analyzed with ImageJ and plotted using graph pad prism 8.0.V, significance was determined using paired t²-test, level of significance was set as “*” $p < 0.05$; “**” $p < 0.01$; “***” $p < 0.001$; “****” $p < 0.0001$, ns- not significant. Schematics were drawn using Biorender.

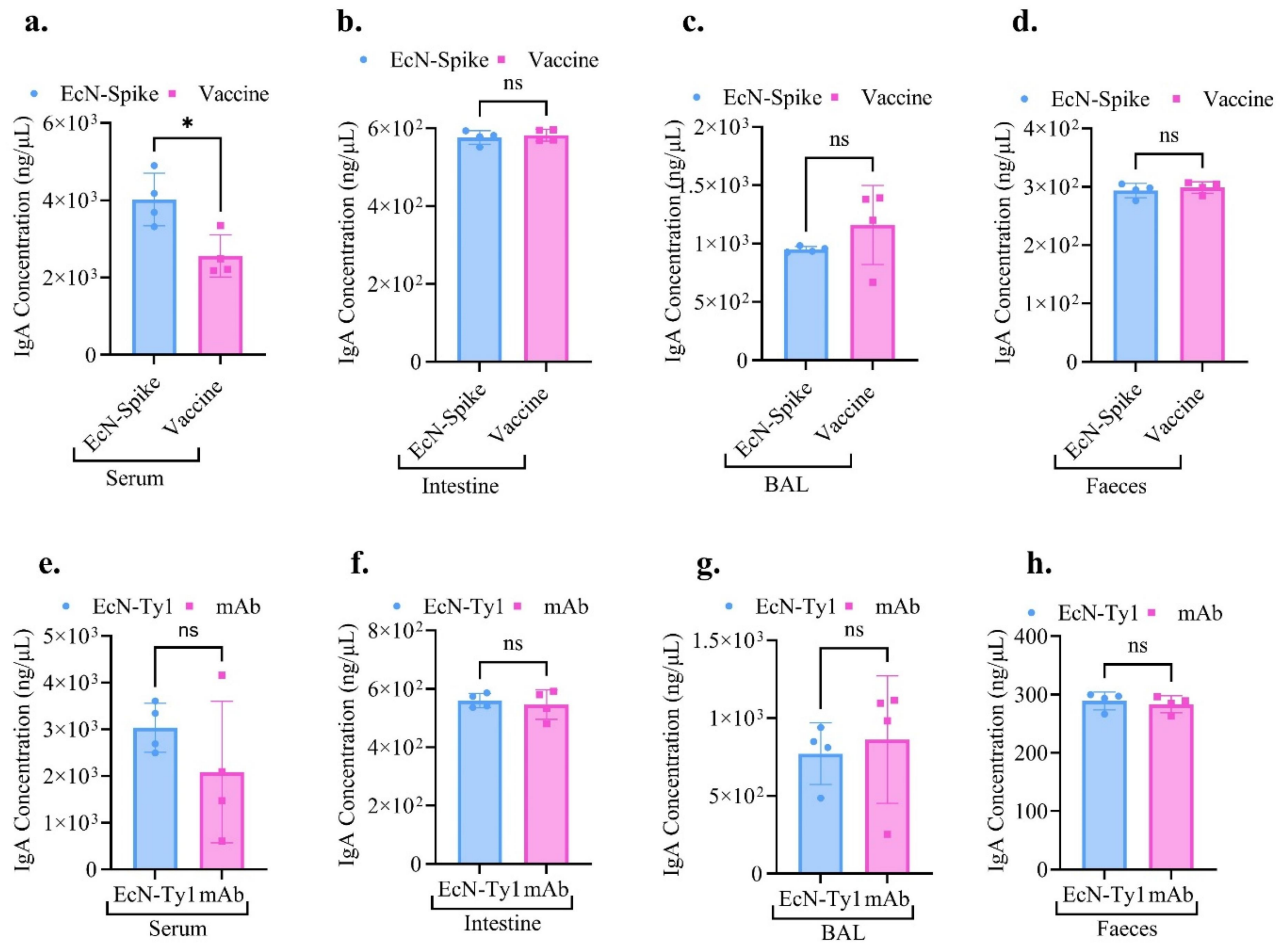


Figure 14. IgA levels in serum, intestine, BAL and faeces. Mice administered with EcN-spike, EcN Ty1 Nb, mRNA vaccine or mAb were analyzed for IgA. The comparative IgA levels in serum (a), intestine (b), BAL (c), faeces (d) of EcN-spike and vaccine groups. The comparative IgA levels in serum (e), intestine (f), BAL (g), faeces (h) of EcN-Ty1 and mAb groups. Graphs are plotted using GraphPad prism 8.0.v, and significance was determined using paired t^2 -test or one-way ANOVA for multiple comparison, level of significance was set as $^{**}p < 0.05$; ns- not significant.

(Figure 15(a)). By the second month (8 weeks), serum IgA levels in the EcN-Spike group remained consistently high (mean $1768.3 \pm 248.4 \text{ ng}/\mu\text{L}$) and comparable to the vaccine group (mean $1920.0 \pm 617.8 \text{ ng}/\mu\text{L}$), indicating sustained systemic immunity. At three months (12 weeks), EcN-Spike-treated mice showed stable IgA levels (mean $1928.7 \pm 567.0 \text{ ng}/\mu\text{L}$), while the vaccine group exhibited higher variability (mean $1810.6 \pm 733.6 \text{ ng}/\mu\text{L}$). By the fourth month (16 weeks), serum IgA levels in the vaccine group surged (mean $7626.8 \pm 2330.3 \text{ ng}/\mu\text{L}$), surpassing the EcN-Spike group (mean $5914.4 \pm 2482.7 \text{ ng}/\mu\text{L}$). This late spike in the vaccine group likely reflects delayed systemic immune activation compared to the consistent response observed with EcN-Spike.

In the BALF, EcN-Spike-treated mice showed higher IgA levels in the first month (mean $510.4 \pm 60.7 \text{ ng}/\mu\text{L}$) compared to the vaccine group (mean $458.5 \pm 42.3 \text{ ng}/\mu\text{L}$) (Figure 15(b)). By the second month, IgA levels in EcN-Spike-treated mice increased significantly (mean $1087.5 \pm 329.2 \text{ ng}/\mu\text{L}$), surpassing the vaccine group (mean $587.8 \pm 136.6 \text{ ng}/\mu\text{L}$). At three months, EcN-Spike-treated mice maintained high IgA levels (mean $984.3 \pm 774.3 \text{ ng}/\mu\text{L}$), though the vaccine group demonstrated a delayed peak (mean $1444.6 \pm 1032.1 \text{ ng}/\mu\text{L}$). At four months, both groups exhibited strong mucosal immunity, with the vaccine group (mean $2765.3 \pm 644.6 \text{ ng}/\mu\text{L}$) slightly outperforming EcN-Spike (mean $2324.3 \pm 643.0 \text{ ng}/\mu\text{L}$).

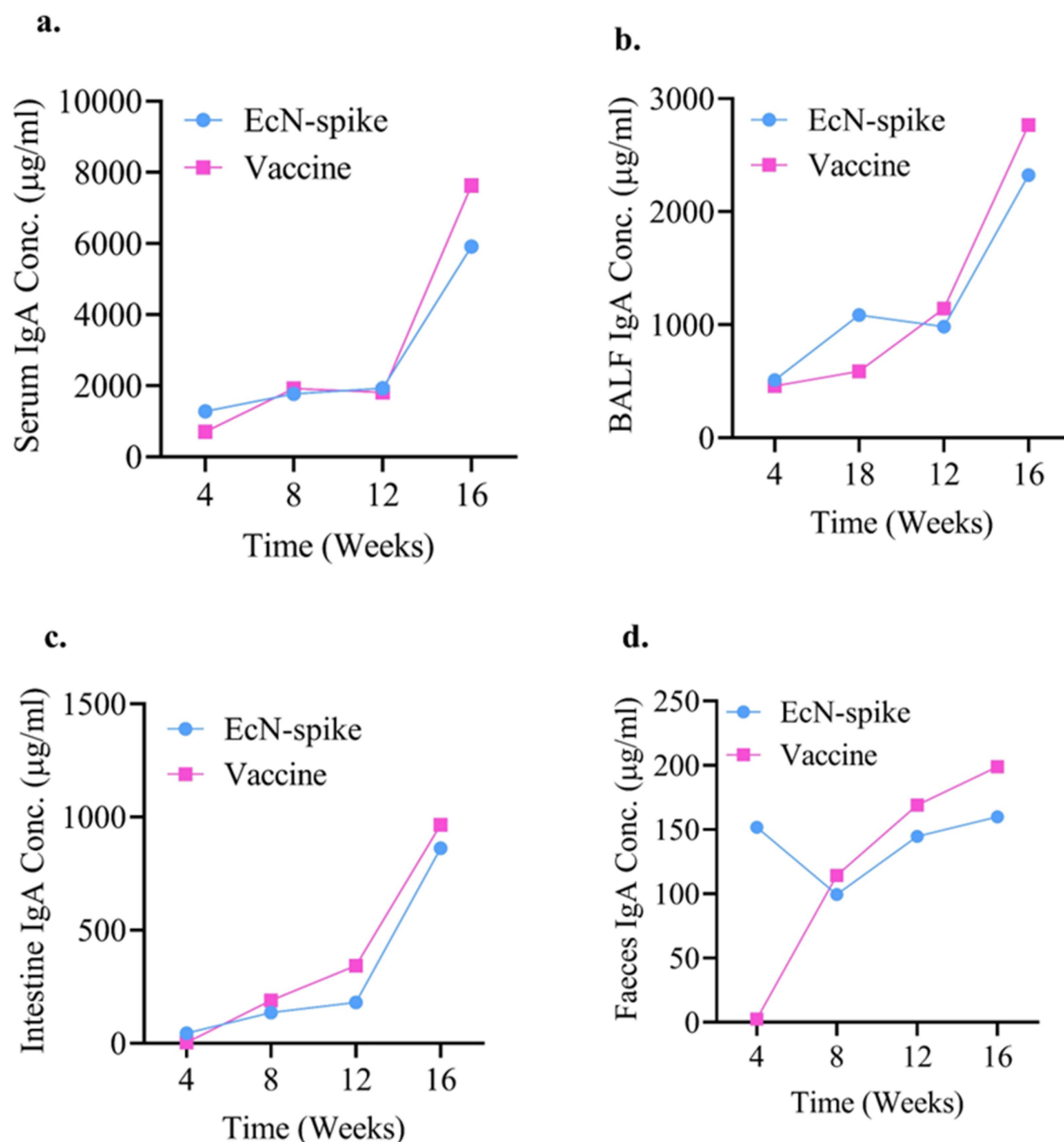


Figure 15. Longitudinal IgA responses across systemic and mucosal compartments.

EcN-Spike-treated mice demonstrated significantly higher intestinal IgA levels at one month (mean $43.8 \pm 19.4 \text{ ng}/\mu\text{L}$) compared to the vaccine group (mean $2.5 \pm 1.3 \text{ ng}/\mu\text{L}$) (Figure 15(c)). This highlights EcN-Spike's ability to rapidly stimulate GI mucosal immunity. Over subsequent months, the EcN-Spike group maintained elevated IgA levels, peaking at $181.1 \pm 77.2 \text{ ng}/\mu\text{L}$ at three months, while the vaccine group showed a delayed response, with increasing levels and variability.

In feces, EcN-Spike elicited a strong IgA response in the first month (mean $151.7 \pm 85.2 \text{ ng}/\mu\text{L}$) compared to the vaccine group (mean 2.5

$\pm 1.3 \text{ ng}/\mu\text{L}$), highlighting its rapid activation of local immunity at the site of antigen delivery (Figure 15(d)). Over the four months, both groups showed comparable levels of fecal IgA, with EcN-Spike stabilizing at $159.5 \pm 23.7 \text{ ng}/\mu\text{L}$ and the vaccine group reaching $198.5 \pm 38.8 \text{ ng}/\mu\text{L}$ by the final month. This convergence suggests that both platforms eventually achieve similar mucosal immunity.

The longitudinal assessment revealed distinct dynamics between EcN-Spike and the Moderna mRNA vaccine in eliciting systemic and mucosal immunity. EcN-Spike induced a rapid systemic and

mucosal IgA response, with early and sustained elevations across compartments, likely reflecting its interaction with gut-associated lymphoid tissue (GALT). This rapid response could be advantageous in providing early protection against mucosal pathogens.

In addition, we monitored the weight and temperature of these mice throughout the duration of experiment and we did not observe any adverse effects (Supplementary Figure S16).

Serum IgA responses highlight systemic immunity (a), BALF IgA concentrations demonstrate respiratory mucosal immune responses (b), Intestinal IgA levels reflect local gut mucosal immunity (c), Fecal IgA levels provide a measure of mucosal immunity in the gastrointestinal tract (d). Data are represented as mean \pm standard deviation ($n = 4$ per group) at each point. Statistical comparisons were conducted using two-way ANOVA for treatment groups (EcN-spike or Vaccine) with pairwise Tukey's post hoc test. $*p < 0.05$, $**p < 0.01$, $***p < 0.001$ compared to EcN-Spike group. Statistical analysis was performed using Graph Pad Prism 8.0.v.

Immune cell profiling of splenocyte subsets following oral and intramuscular immunization

To evaluate the immune responses elicited by different immunization strategies, splenocytes from mice administered with EcN-Spike or the mRNA vaccine were analyzed using flow cytometry. Cellular populations were characterized for markers CD3 (T cells), CD4 (Helper T cells), CD8a (Cytotoxic T cells), CD11c (Dendritic cells), CD56 (Natural Killer cells), and CD68 (Macrophages) at three months post-immunization. EcN-Spike-treated mice showed variable but generally elevated percentages of CD3⁺ cells (T cells) ranging from 19.88% to 46.27%, compared to the vaccine group's range of 22.14% to 84.30%, which exhibited a decreasing trend (Figure 16(a)). CD4⁺ cell percentages were consistent across groups, with EcN-Spike (15.16–20.89%) closely matching vaccine-treated mice (16.62–22.21%) (Figure 16(b)). EcN-Spike elicited robust CD8a⁺ cell (Cytotoxic T cell) responses (15.90–23.31%), comparable to the vaccine group (13.80–30.83%) (Figure 16(c)). Macrophage activation, as indicated by CD68⁺ cell percentages, was

similar between EcN-Spike (15.90–25.65%) and the vaccine group (19.64–43.91%) (Figure 16(d)). EcN-Spike also induced consistently higher percentages of CD56⁺ cells (Natural Killer cells) (9.09–13.09%) compared to the vaccine group (4.73–20.24%), which showed substantial variability (Figure 16(e)). Finally, EcN-Spike-treated mice exhibited higher CD11c⁺ (Dendritic cell) percentages (6.78–30.07%) compared to the vaccine group (10.85–29.54%), suggesting stronger antigen-presenting cell activation (Figure 16(f)). These results suggest that EcN-Spike stimulated robust responses in adaptive immune populations, including T cells (CD3⁺), Helper T cells (CD4⁺), Cytotoxic T cells (CD8a⁺), and antigen-presenting cells (CD11c⁺). This suggests that EcN-Spike effectively activates both adaptive and antigen-presenting cell populations. Moreover, EcN-Spike consistently elicited higher levels of Natural Killer cells (CD56⁺), indicative of enhanced innate immunity. These results highlight EcN-Spike's ability to elicit a balanced immune response, combining adaptive and innate components.

Flow cytometry analysis show the percentages of the following cell populations in third month: CD3⁺ T cells (a.), CD4⁺ Helper T cells (b.), CD8a⁺ Cytotoxic T cells (c.), CD68⁺ Macrophages (d), CD56⁺ Natural Killer cells (e), CD11c⁺ Dendritic cells (f.). The data are presented as mean \pm SEM for each group ($n = 4$). Statistical comparisons between groups were performed using two-way ANOVA with Tukey's post hoc test ($*p < 0.05$, $**p < 0.01$, $***p < 0.001$).

Evaluation of cellular immune responses following introduction of the bacterial delivery vehicle

Next, we evaluated the CD8⁺ and CD4⁺ profiles in serum, intestine, BAL and feces. In evaluating the CD8⁺ T cell levels, we observed that the EcN-Spike group displayed significantly higher levels of CD8⁺ T cells in serum compared to the EcN-Ty1, mAb and mRNA vaccine groups (Figure 17(a-d); Supplementary Figure S17, Supplementary Table 6). This marked increase in CD8⁺ T cell levels in the EcN-Spike group indicates a strong cellular immune response, likely driven by the efficient antigen presentation of the spike protein by the engineered bacteria on the cell surface. CD4⁺ T cell analysis

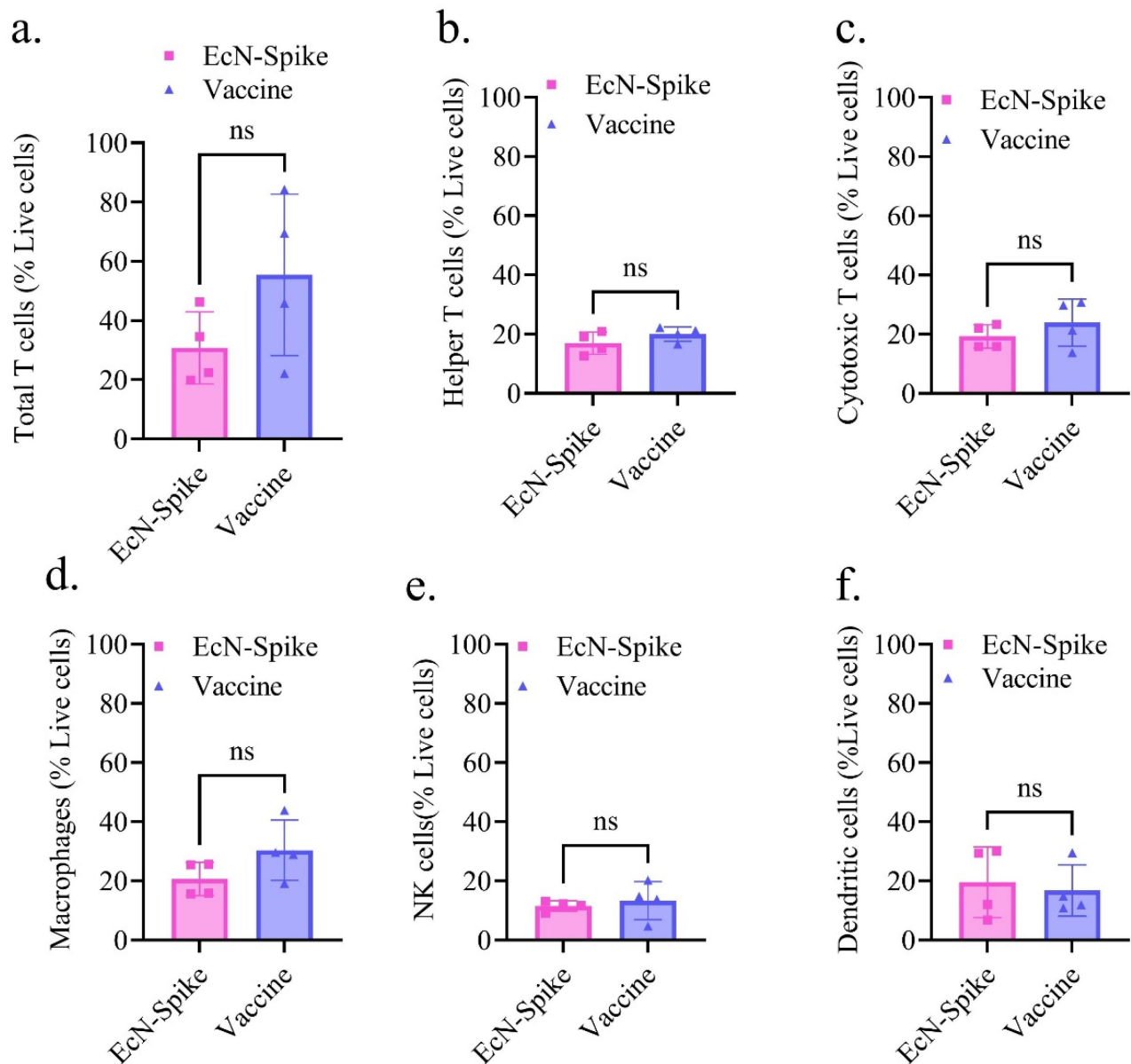


Figure 16. Analysis of splenocyte subsets in mice following oral and intramuscular immunization.

revealed a significantly lower level of $CD4^+$ T cell levels in the serum of animals treated with EcN-Ty1 compared to mAb (Figure 17(e)). However, no significant differences in $CD4^+$ T cell levels were detected in the intestinal fluid (Figure 17(f)), BAL fluid (Figure 17(g)), or feces (Figure 17(h)) of these groups. Likewise, EcN-Spike and the mRNA vaccine treated groups showed no significant differences in $CD4^+$ T cell levels across the serum (Figure 17(i)), intestinal fluid (Figure 17(j)), BAL fluid (Figure 17(k)), or feces (Figure 17(l)). The consistent $CD4^+$ levels across

these groups suggest that the immune response remains balanced, and that the introduction of the bacterial vehicle does not adversely affect the host immune system, indicating a healthy immune profile (Supplementary Figure S18, S19).

Bacterial toxicity and persistence

Cytokines and chemokines are key extracellular signaling molecules that mediate cell-cell communication, playing critical roles in cellular growth, differentiation, gene expression, migration,

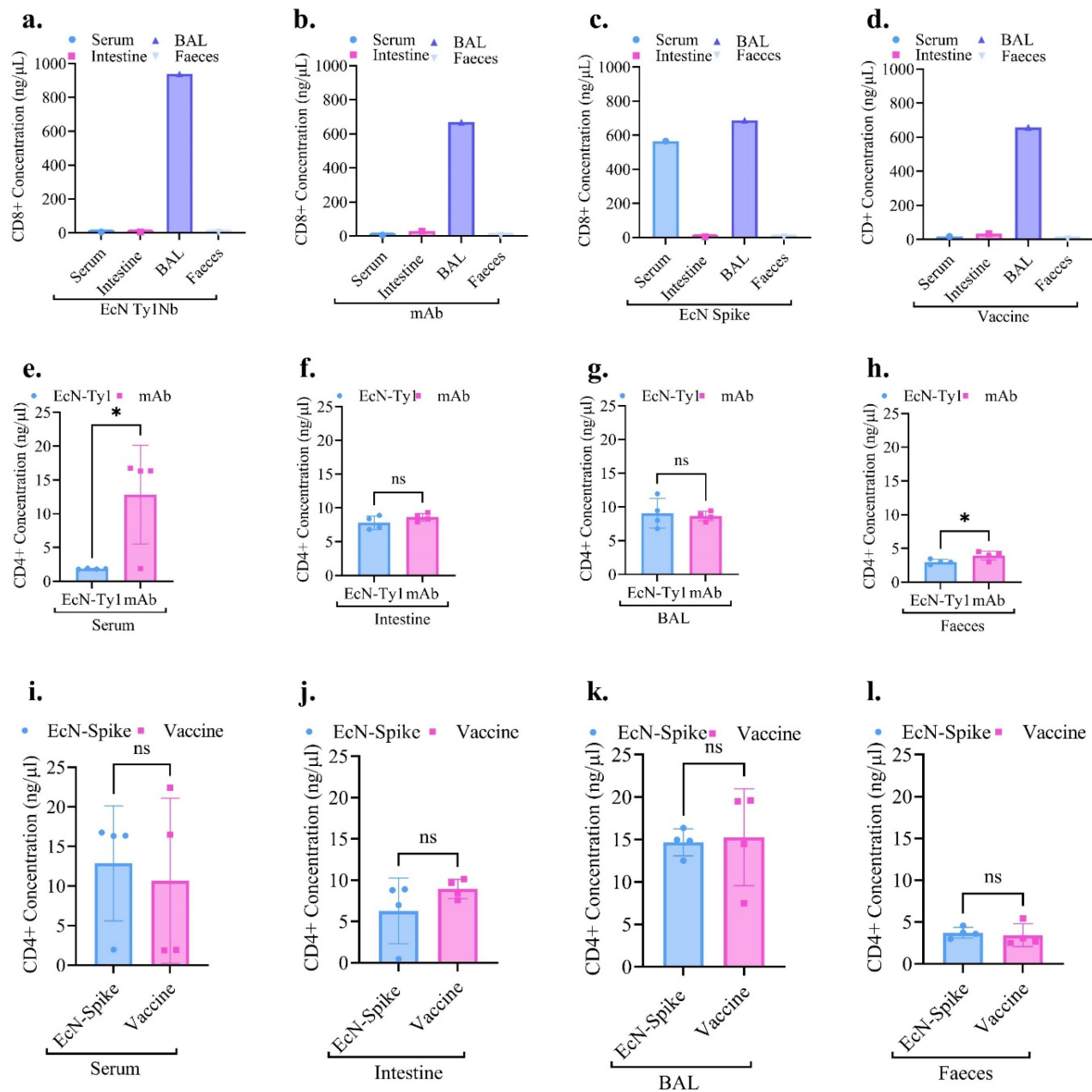


Figure 17. CD8⁺ and CD4⁺ levels in serum, intestine, BAL and faeces. The CD8⁺ concentrations found with ELISA in serum, intestine, BAL and faeces of EcN-spike (a), vaccine (b), EcN Ty1 Nb, and mAb (d) given animals. Mice administered with EcN-Ty1 Nb, mAb, or EcN-spike and mRNA vaccine were also analyzed for CD4⁺ levels with ELISA. Comparative CD4⁺ levels in serum (e), intestine (f), BAL (g), faeces (h) for EcN Ty1 Nb vs mAb groups. Comparative CD4⁺ levels in serum (i), intestine (j), BAL (k), faeces (l) of EcN-spike vs vaccine groups. Graphs are plotted using GraphPad prism 8.0.v, and significance was determined using paired t²-test or one-way ANOVA for multiple comparison, level of significance was set as *ns* $p < 0.05$; ***** $p < 0.01$; ****** $p < 0.001$, *ns*- not significant.

immunity, and inflammation. The results indicated that EcN-Spike and the vaccine elicited similar cytokine profiles, including c5/c5a, M-CSF, ICAM-1, and SDF-1, with notable differences such as higher ICAM-1 levels in EcN-Spike treated mice, suggesting heightened T-cell activation (Figure 18, a). In the intestine, the vaccine group showed elevated IL-1 α levels compared to EcN-Spike (Figure 18(b)), which

is crucial for initiating inflammatory responses. Similar cytokine trends were observed in BAL samples, except for the detection of SDF-1 in the feces of vaccinated animals (Figure 18, c-d), suggesting localized recruitment of immune cells. Comparing EcN-Ty1 and mAb groups, we found elevated serum ICAM-1 levels in the EcN-Ty1 group (Figure 18(e)), indicative of T-cell activation (Supplementary Figure

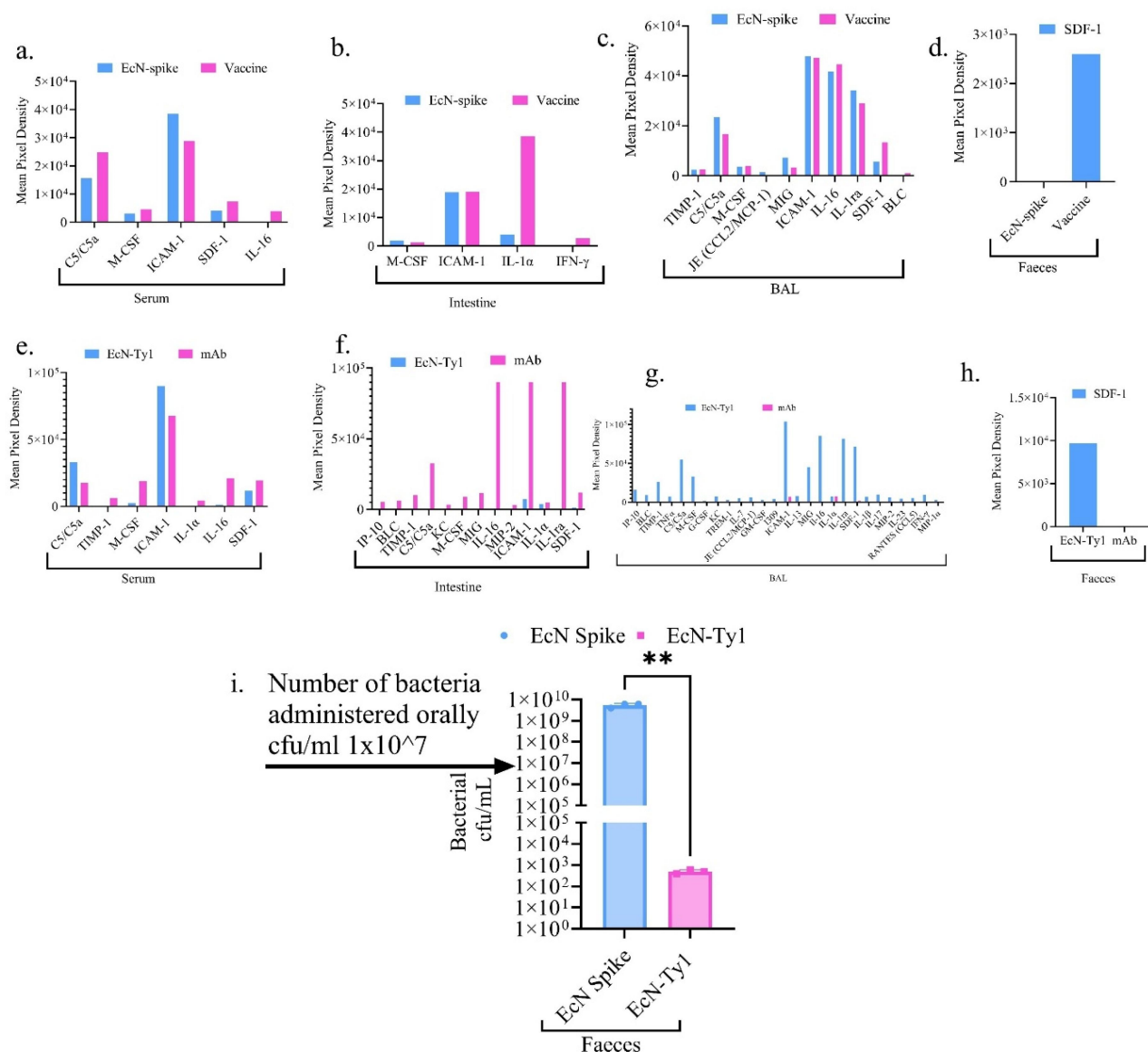


Figure 18. Cytokine profiling in mice administered with live bacteria, vaccine or mAb. EcN-spike was compared to mRNA vaccine for relative changes in cytokines and chemokines in serum (a), intestine (b), BAL (c), and faeces (d). EcN-Ty1 Nb were compared with mAb and similarly compared for cytokines and chemokines in serum (e), intestine (f), BAL (g) and faeces (h). For bacterial persistence faeces were collected after 5 days of administration and cfu/mL was calculated using serial plate dilutions (i). Densitometry performed with LiCOR-image studio and values were plotted using GraphPad prism 8.0.v, and significance was determined using paired t^2 -test or one-way ANOVA for multiple comparison, level of significance was set as $^{**}p < 0.05$; $^{***}p < 0.01$; ns- not significant.

S20, Supplementary Table 7). In the intestines, no significant cytokine or chemokine differences were observed (Figure 18(f)). However, BAL samples from EcN-Ty1-treated mice showed higher levels of ICAM-1, IL-16, IL-1ra, MIG, and SDF-1 compared to mAb-treated mice (Figure 18(g)), indicating enhanced immune activation and modulation. IL-1ra is an anti-inflammatory cytokine, while MIG recruits activated T cells. Elevation of SDF-1 suggests

enhanced immune cell recruitment and retention. Elevated SDF-1 was also detected in the feces of EcN-Ty1-treated animals (Figure 18(h)). These findings further suggest that the bacterial host, whether expressing spike protein or nanobodies, does not induce significant inflammatory or toxic effects in the host organism, as inferred from similar expression profiles and the absence of overtly inflammatory cytokines (Supplementary Figure S20, Supplementary Table 7).

Further investigation into bacterial recovery from feces revealed that approximately 5.0×10^9 CFU/mL of EcN-Spike and 6.0×10^3 CFU/mL of EcN-Ty1 were recovered, starting from an initial dose of 1×10^7 bacteria administered via oral gavage (Figure 18(i) Supplementary Figure S21). The longer and higher persistence of EcN-Spike in the gut compared to EcN-Ty1 is likely multifactorial, involving a combination of immune evasion or modulation, differences in immune activation, bacterial fitness, metabolic burden, microbial interactions, and potential changes in adhesion properties. These factors can collectively influence the stability, survival, and colonization efficiency of the engineered bacteria within the gut environment. Further studies are necessary to elucidate the specific mechanisms behind these observations.

Discussion

The human microbiota represents a vast, primarily unexplored area for short-term immunotherapy and long-term adaptive immunity against viruses.^{43,44} Probiotic bacteria offer protection against pathogens in the gastrointestinal (GI) tract through direct antagonism, competitive exclusion, barrier function, and immune stimulation due to their proximity to Dendritic cells (DCs).^{45,46} These intestinal DCs, also called Langerhans cells, are among the first cells to encounter pathogens in the GI tract, activating and migrating to lymph nodes to initiate protective immune responses.^{43,47} Although commensal bacteria and natural probiotics have some capacity to present antigens to DCs, their ability is limited as they lack the means to capture and present antigens effectively.^{44,47} In the case of SARS-CoV-2, the natural defenses are overwhelmed, leading to severe morbidity and mortality.^{48–50}

In response, we propose leveraging live, programmable bacteria to deliver therapeutic nanobodies and viral antigens, potentially enhancing outcomes in viral infections and modulating the immune system. Our choice of EcN as a delivery vehicle is due to its genetic malleability, probiotic status, distinction from pathogenic *E. coli* strains, and nonpathogenic nature.^{6,22,51,52} We engineered EcN to express anti-spike nanobodies using Intimin and Lpp-OmpA as surface anchors,

ensuring efficient antigen presentation, direct interaction with host cells, and nanobody-mediated neutralization.⁵³ These nanobody-bearing EcN constructs successfully inhibited the interaction of spike protein-expressing pseudoviruses with the ACE2 receptor. This demonstrates the potential of using modified probiotics to prevent the early stages of viral infection.

The neutralization assays revealed that while both EcN-Ty1 and mAb effectively inhibited pseudovirus-ACE2 interactions, EcN-Ty1 showed a unique cytokine profile, including elevated levels of ICAM-1, IL-16, IL-1ra, MIG, and SDF-1, particularly in the bronchoalveolar lavage (BAL). These cytokines play critical roles in T-cell activation (IL-16), inflammation regulation (IL-1ra), and immune cell recruitment (MIG and SDF-1), suggesting that EcN-Ty1 not only triggers a robust immune response but also modulates it to prevent excessive inflammation. This balanced response is indicative of a potentially safer therapeutic profile, minimizing the risk of cytokine storm, a concern with some conventional antibody treatments.

Moreover, although several secretion systems such as Type I, Type II, Type III (Sec dependent and Tat-dependent) exists in Gram-negative bacteria which can be used for delivering nanobodies to the gut, they have limitations such as rapid proteolytic degradation of exported protein and/or being less efficient in targeting distal organs such as lungs and bloodstream. Instead, we utilized OMVs as a novel delivery system for these nanobodies. Bacterial OMVs are nanosized vesicles involved in cellular communication.³⁷ By surface-expressing nanobodies, we designed a bacterial system capable of distributing anti-spike nanobodies through OMV-mediated translocation to the systemic circulation, potentially mitigating disease onset and providing time for the host system to mount an immune response. Although the potential immunogenicity of OMVs poses a risk, genetic modifications to reduce LPS levels could mitigate this.⁵⁴ Our results show that OMVs effectively transported nanobodies across the gut-blood barrier possibly via M-cell transcytosis, enterocytes endocytosis or DC uptake, indicating their potential as a delivery system for therapeutic agents.

Current vaccine technology typically addresses pathogens that have already surpassed mucosal

barriers, resulting in limited cellular immunity and weak protection at mucosal barriers.^{9,10,55} In contrast, vaccination at mucosal surfaces induces cell-mediated immune responses while simultaneously generating a systemic antibody response.^{14,56,57} Hence, we engineered EcN to express the spike protein, demonstrating that orally administered EcN-spike in mice triggers both systemic and mucosal immunity. This was evidenced by the significant increase in IgA levels in serum and the enhanced presence of T cells and monocytes in the intestines of mice administered with EcN-spike.

The IgG and IgA profiling also showed that EcN-Spike led to higher IgA levels in serum compared to the mRNA vaccine, indicating a stronger mucosal immune response. The comparison between EcN-Spike and the mRNA vaccine also revealed distinct temporal patterns in immunity. While the vaccine induced a strong systemic IgA surge in later months, EcN-Spike excelled in early and sustained mucosal responses. This is particularly significant as mucosal immunity plays a crucial role in preventing respiratory infections, including SARS-CoV-2, at their point of entry. The presence of sustained IgA levels suggests that EcN-Spike could provide prolonged protection at mucosal surfaces, which is a limitation of many current vaccines that primarily induce systemic immunity. Furthermore, the persistence of spike protein in the gut, coupled with the detection of cytokines such as ICAM-1, highlights the probiotic's ability to maintain a durable immune response, possibly through immune evasion or modulation mechanisms conferred by the spike protein.

The analysis of both CD8⁺ and CD4⁺ T cells is vital for understanding the overall immune response, as CD8⁺ T cells are key in targeting and eliminating infected cells, while CD4⁺ T cells play a central role in orchestrating the immune response. The significant increase in CD8⁺ T cell levels in the EcN-Spike group underscores the platform's ability to elicit a potent cellular immune response, which is crucial for effective viral clearance and long-term immunity. The observed CD4⁺ T cell levels, with no significant differences across mucosal sites, support the conclusion that the engineered probiotic platform activates the immune system effectively without causing detrimental inflammation or immune dysregulation.

The elevated cytokine expression unique to EcN-Spike and EcN-Ty1, such as IL-16 and IL-1ra, suggests a distinct immunomodulatory capability of these engineered probiotics. IL-16's role in T-cell activation and IL-1ra's anti-inflammatory properties highlight the potential for these probiotics to not only activate the immune response but also regulate it, reducing the risk of adverse effects associated with excessive immune activation.

Crucially, the observed increase in antibody titers following repeated oral administration of EcN-spike suggests the potential for developing a live bacterial vaccine.^{9,10} Such a vaccine could be more stable, cost-effective, and easier to administer than current vaccines, especially in regions where cold-chain storage is challenging.^{58,59}

In conclusion, our study offers further insights into the use of engineered probiotics as delivery vehicle for nanobodies and viral antigens, an advancement over single-function approaches, coupled with the novel application of OMVs, for immunotherapy against viral infections. The ability of EcN-Spike to activate both CD4⁺ and CD8⁺ T cells, coupled with consistent dendritic cell activation, suggests that it effectively bridges innate and adaptive immune pathways, which underscores the potential of engineered probiotics as versatile platforms for vaccine development. The comparison with traditional mAb and mRNA vaccines highlights the unique benefits of probiotic-based therapies, including the potential for enhanced mucosal immunity and a safer cytokine profile. We envision this platform playing multiple roles – from neutralizing initial infection stages to providing long-lasting immunity against various viruses. Our OMV-based nanobody delivery system represents a novel method for *in situ* delivery, with bacteria and OMVs displaying viral antigens and anti-antigen nanobodies forming a versatile, efficient platform for experimental vaccine and therapeutic agent production.

However, our study is not without limitations. The absence of a live SARS-CoV-2 disease model due to BSL-3 constraints limits our ability to fully validate the real-world effectiveness of this approach. Future research should focus on immune correlates and effectiveness in real-world scenarios to better understand these vaccines' protective mechanisms. Although the

observed differences in immune responses could be due to variations in vaccine dose or dosing intervals, our findings hint at nuanced differences in the humoral response elicited by engineered probiotics. Future studies should also focus on optimizing these probiotic platforms to enhance immune responses while minimizing potential risks. The long-term persistence of bacteria in the gut, while beneficial for sustained immune activation, requires further investigation to ensure safety. It can be achieved by means of containment strategies such as auxotrophic dependencies and suicide switches, however efficacy with techniques such as 16s rRNA sequencing on fecal microbiota before and after EcN administration to track shifts in microbial diversity will be important. Moreover, while our data indicates that there is a potential gut-brain axis in the context of OMV-mediated drug delivery, this phenomenon needs further exploration, including a thorough investigation into potential toxicity to the brain. It is speculative that OMVs may transverse blood-brain barrier via adsorptive-mediated transcytosis, monocyte trafficking or tight junction modulation. To optimize OMVs for organ-specific targeting, future engineering approaches include surface functionalization with tissue-specific ligands, LPS detoxification for systemic safety and fusion protein incorporation for enhanced targeting. It is also important to note that the interaction between engineered probiotics and the host's microbiome is complex and can be significantly influenced by antibiotic treatment. In cases where antibiotics specifically target Gram-negative bacteria, the persistence of engineered EcN strains may be compromised, reducing the duration and level of antigen or nanobody presentation. Conversely, a reduction in competing gut microbes might allow for more effective colonization and higher levels of antigen expression. The net effect of these changes depends on the specific antibiotics used and their spectrum of activity. Understanding these dynamics is crucial for optimizing the administration of vaccines and biologics, particularly in individuals undergoing antibiotic therapy.

The harsh conditions of the stomach (low pH) and intestines (digestive enzymes, bile salts) could

potentially degrade antigens before reaching target sites. Differences in gut microbiota and host physiology may also lead to individual variations in vaccine efficacy. Engineered EcN is typically transiently colonized, requiring strategies to ensure sustained antigen exposure.

To overcome these challenges, formulating EcN within acid-resistant capsules or hydrogel coatings to shield bacteria from gastric degradation could be employed. Using OMV-based delivery, which naturally protects antigens from enzymatic breakdown could also be explored further. Additionally, the exploration of different dosing regimens such as bacterial concentration, dosing intervals, booster strategies and formulations could further refine these platforms for broader application against various viral pathogens.

Regulatory challenges also exist, such as requiring extensive biosafety evaluations, including potential risks of uncontrolled colonization, gene transfer, and environmental impact. Engineered *E. coli* strains must demonstrate genetic stability to prevent unintended mutations affecting safety or efficacy. While some live bacterial therapies (e.g., *Lactococcus lactis* for inflammatory diseases) have been evaluated, oral bacterial vaccines remain in early regulatory stages, necessitating further clinical validation and risk assessments. We anticipate that our research will pave the way for further exploration of live bacteria as vaccine platforms against enigmatic emerging and cryptic diseases.

Methods

Bacterial strains and culture growth conditions

E. coli Nissle 1917 (*EcN*) strain was used for the construction of all the bacterial strains bearing nanobodies. All the strains were grown in LB broth or on LB agar plates, supplemented with appropriate antibiotic- Ampicillin ($100\mu\text{g mL}^{-1}$), Chloramphenicol ($50\mu\text{g mL}^{-1}$), or Kanamycin ($100\mu\text{g mL}^{-1}$). Prior to assaying protein expression with SDS-PAGE Western blot analysis, Fluorescence microscopy, and Spike-ACE2 inhibition assays, fresh media was inoculated with bacterial cultures from an overnight liquid culture. All the bacterial cultures were grown at 37°C and 200rpm.

Proteomics analysis with mass spectrometry

Bacteria were grown as previously for proteomics analysis. In brief, 1% of overnight cultures were inoculated into 100mL of fresh LB broth supplemented with the appropriate antibiotic and identically grown at 37°C and 200rpm until OD₆₀₀ reached 0.9–1.0 (approx. 3.00–6.00hr.). Cultures were spun at 4°C for 15min, 3500×g and cells were resuspended in 5–10 volumes of the Bacterial cell lysis buffer (Gold Bio), supplemented with DTT and EDTA (5mm), and Lysozyme (40mg/mL), DNase (800 U/mL) and RNase (24 U/mL). Following vortexing, and 5min incubation on ice, suspensions were incubated at 37°C for 60 min and lysates were centrifuged at 20,000×g, 4°C for 30min, and the clear lysate was collected and quantified using BCA assay (Thermo Scientific).

Protein samples were dried in a speed vac and resuspended in TEAB buffer according to standard *in-solution* digestion protocol. Samples were reduced with TCEP (tris-(2-carboxyethyl) phosphine) and alkylated with MMTS (methylmethane-thiosulfonate). Samples were digested overnight at 37°C and reactions were stopped by adding 10% formic acid. These samples were dried and resuspended in 0.1% formic acid. 5μL (~1μg) of each sample was analyzed by NanoLC-MS/MS (Orbitrap Eclipse) and was searched against a combined database consisting of the *E. coli* Nissle 1917 database accessed from the Biocyc.org website and a database containing the nanobody sequences using Proteome discoverer *ver* 2.4 and the Sequest HT search algorithm using standard LFQ workflow (Thermo scientific).

Cell culture conditions

The metastatic triple negative murine breast cancer 4T1 cells (ATCC CRL-2539, passage number 5 to 15), CaCo2 (passage number 5 to 15), and HEK293 (passage number 5 to 15), cell lines were cultured using RPMI media (Gibco #21875034) containing 10% Fetal Bovine Serum (Gibco #26140079) and 5% Penicillin-streptomycin (Gibco #15070063). 293T-hACE2 (Abnova Cat# KA6152) cell lines were cultured using DMEM media supplemented with 10%

FBS. Cells were maintained at 37°C with 5% CO₂ in air and sub-cultured 2 times a week, unless otherwise stated.

Recombinant DNA techniques

Plasmids generated during this study are listed in Supplementary data: Figure S1 and S2. High fidelity and diagnostic polymerase chain reactions (PCR) were performed using Phusion High Fidelity polymerase (New England Biolabs) and DreamTaq DNA Polymerase (Thermo Scientific), respectively. Geneblocks (GeneArtSynthesis) and custom primers (Integrated DNA technologies) used are listed in Supplementary data: Table S7, S8. Anti-COVID-Nanobody expressing genetic constructs with Intimin and Lpp-OmpA surface display signals were designed, synthesized from GeneArtSynthesis® (Thermo Scientific) and Integrated DNA Technologies (IDT Inc.), and then incorporated into CJ23105 plasmid backbone using DNA2.0 and Snap Gene® Viewer4.1.8. These plasmids are listed in Supplementary data: Figure S3, Table S9. All restriction digests and ligation reactions were carried out using NEB restriction enzymes and T₄ DNA ligase (New England Biolabs). Following completion of ligation, reaction mixtures were chemically transformed into NEB DH5α cells (New England Biolabs), as per the manufacturer's instructions.

SDS-PAGE and Western immunoblot analysis

Following cell growth for expression assays, 1.00D unit of cultures samples were centrifuged at 16,000×g for 15min to ensure separation of cells and supernatant. Supernatant fraction was prepared by using 10% v/v Trichloroacetic acid precipitation method followed by washing with ice-cold Acetone.⁶⁰ Both the precipitated supernatant and cell pellets were resuspended in 2×SDS loading buffer (10mL Glycerol, 1g SDS, 0.1g Bromophenol Blue, 200mm DTT to a volume of 50mL in 100mm Tris-HCL, pH6.8) to a final volume of 50μL and 200μL, respectively. Both these cell fractions and supernatants were subjected to SDS-polyacrylamide gel electrophoresis (SDS-PAGE).

Gels were Coomassie stained with Instant Blue (Expedeon™), Silver stained with Pierce™ Silver stain kit (Thermo Fisher Scientific) or prepared for Western immunoblotting by electro-transfer onto Nitrocellulose membrane (GE Healthcare Life Sciences). Blots were blocked using 3% w/v bovine serum albumin (BSA) in TBS buffer (24 gL⁻¹ Tris Base, 88 gL⁻¹ NaCl and 0.1% v/v Tween). Primary antibodies were diluted in 1:1000 using TBS-Tween. All blocking steps were carried at 4°C overnight unless otherwise stated, while incubation steps were carried out at 2hr unless otherwise stated. Western immunoblots were visualized using Pierce®ECL Western Blotting Substrates (Thermo Scientific) and ChemiDoc™ Imaging system (BioRad). All antibodies used in this study are listed in Supplementary Table 10.

SARS-CoV-2 spike protein -ACE2 receptor binding inhibition assay

EcN harboring 4- nanobodies expressing constructs, namely 1. pInt-Ty1, 2. pInt-VHH72, 3. pLpp-OmpA-Ty1 and 4. pLpp-OmpA-VHH72 along with wild-type *E. coli* Nissle 1917 as a control were grown in fresh LB broth as mentioned earlier. These cultures were then centrifuged at 4°C for 10 min at 8400×g and cells were washed twice with 1XPBS, centrifuged, and resuspended in 10μL of 1XPBS. All the reagents were brought to room temperature (RT) (18–25°C) before use and reactions were run in triplicates. Test samples for Nanobody inhibiting Spike protein-RBD and ACE2 receptor interaction were prepared as below. Briefly, 2mL of Nanobody expressing cultures along with wild-type WT-*EcN* were normalized to OD₆₀₀=1.0 Unit. Cultures were centrifuged twice at 8400rpm for 15min and resuspended in 1mL of 1XPBS. Stock solution of test reagent was prepared by mixing 75μL Bacterial cell suspension in 1XPBS, 7.5μL, 50X ACE2 protein concentrate and 292.5μL 1×Assay diluent, for preparing sample enough for triplicates. The following dilutions were prepared by using 37.5μL previous sample and adding into 337.5μL, 1×ACE2 protein working solution, while positive control was prepared by using only 375μL, 1× ACE2 protein working solution, for triplicates at 100μL per well.

Spike-RBD coated 96-well plate was labeled and 100μL each of Test reagent sample was added into appropriate well, covered with plate sealing film and incubated overnight at 4°C with gentle shaking. The following day, the solution was discarded, washed 4× times with 1× wash solution and added with 300μL of 1× wash buffer for 5min and liquid was completely removed. After the last wash, residual 1× wash buffer was removed with decanting or aspirating and added with 100μL of 1× Detection Antibody and incubated 1hr at RT. After incubation, the solution was discarded and wash steps were repeated 3× times, as previously. Plate was then added with 1× Anti Goat HR-conjugated IgG antibody to each well and incubated for 1hr at RT. Solution was discarded, and wash steps were repeated as previously for 4× times. Each well was then added with 100μL of TMB One-Step substrate Reagent and incubated for 30min at RT in dark. It was added with 50μL of Stop Solution and absorbance was read at 450nm, using *EnVision* 2102 Multilabel Reader (Perkin Elmer).

Development of an assay for surface nanobody detection

EcN were freshly transformed with nanobody expressing plasmids and grown along with WT-*EcN* as a control. All cultures were grown identically in 10mL LB medium using an overnight culture and supplemented with appropriate antibiotic for ~3.00hr or until OD₆₀₀ reached 0.9–1.0. All the centrifugation steps were carried out at 3500×g for 15 min, at RT, unless otherwise stated. OD₆₀₀, 1Unit samples from each culture were centrifuged and pellets were resuspended in 1mL of Phosphate Buffered Saline (1XPBS). It was centrifuged and pellets were re-suspended in 200μL of 1XPBS and added with 1μg of Spike Protein (carrier-free Recombinant SARS-CoV-2 S Protein (S1+S2) (Bioline #793706)) and incubated in the dark for an hour at RT. Following centrifugation, it was resuspended in 1 mL of 1XPBS and centrifuged again, and pellets were resuspended into 200μL of 1XPBS. It was then added with 1μg of Purified anti-SARS-CoV-2 Protein S2 antibody (Bioline #943202), that specifically binds to S2 fragment of Spike protein. This whole reaction was incubated

in the dark for 30min. It was centrifuged and resuspended into 1mL of 1XPBS as previously and centrifuged. Following this, pellet was resuspended into 200µL of 1XPBS and added with secondary antibody (Alexa Fluor[®] 647 anti-mouse IgG2b, Bioline #406715). Following 30min of incubation in dark, the reaction tubes were centrifuged twice, and pellet were resuspended into 200µL of 1XPBS. It was placed into a transparent 96-well (Corning[®]) plate and read for the fluorescence using a fluorescent microscope (Leica Microsystems).

Competitive exclusion assay to evaluate nanobody catalyzed inhibition of spike-RBD-ACE2 receptor binding using CaCo2 and 4T1 cell lines

CaCO₂, HEK293FT, and 4T1 cell lines were used for the nanobody detection assay. Cell lines were grown in respective media (ATCC) using an 8-chamber slide (Ibidi), until confluency by incubating at 37°C with 5% CO₂. The cell media were removed, and cells were washed 3× times with 1XPBS. Cells were fixed using 4% formaldehyde (Fisher Brand) by incubating for 10min at RT. The formaldehyde was drained, and cells were washed 3× times to remove the residual formaldehyde. It was followed by permeabilization. Cells were permeabilized with permeabilization buffer (0.1% TritonX100 in 1XPBS) and incubated for 10min at RT, followed by 3× washes with 1XPBS. Cells were then blocked using blocking buffer (3% BSA in 1XPBS with 0.1% TritonX100) for 30min at RT. Following buffer removal, cells were added with primary antibody and/or Spike protein prepared in 0.1% TritonX 100, with 30mg/mL of BSA (Filter sterilized). Primary antibody (Anti-ACE2 (E-11): sc -390,851 (Santa Cruz Biotechnology Inc.) was added for 1–2hr at RT followed with 3× washes with wash Buffer (0.1 % TritonX100 in 1XPBS) (15min washing with 5min in between). It was followed with secondary antibody (Alexa Fluor[®] 647 anti-mouse IgG2b, Bioline #406715) prepared in 1XPBS (0.1% Tritonx100 with 30mg/mL BSA).

When spike protein was utilized, following the blocking step, and/or Anti-ACE2 washing step, cells were added with 1µg of Spike Protein

(carrier-free Recombinant SARS-CoV-2 S Protein (S1+S2) (Bioline #793706)) and incubated in dark for an hour at RT. Following 3× washes with washing buffer, 1µg of Purified anti-SARS-CoV-2 Protein S2 antibody (Bioline #943202) was added, that specifically binds to S2 fragment of Spike Protein. The whole reaction was incubated in dark for 30 min. Following 3× washes with washing buffer, secondary antibody (Alexa Fluor[®] 647 anti-mouse IgG2b, Bioline #406715) was added. After 30min of incubation in dark, cells were washed 3× times with washing buffer and were visualized for fluorescence, using a fluorescent microscope (Leica Microsystems) at The Live Microscopy Imaging Core, The University of Cincinnati.

Isolation and characterization of outer membrane vesicles (OMV)

For the isolation of bacterial outer membrane vesicles (OMV) a sequential differential centrifugation protocol was developed.²² In brief, anti-COVID nanobody bearing *EcN* along with WT-*EcN* were grown overnight at 37°C and 200rpm. 1.0% of these cultures were inoculated in 1.0L of fresh LB Broth, supplemented with appropriate antibiotic. Cultures were grown until OD₆₀₀ of ~1.5 Unit. Culture was cleared of bacteria by centrifugation (8000×g, 4°C, 15minutes) followed by concentrating the supernatant using Pierce Protein Concentrators (30kDa, ThermoFisher #88531). 70mL of the concentrated supernatant was then ultracentrifuged at 91,000×g for 4.0hr. The pellet obtained was resuspended in 1XPBS, pH7.4, followed by washing with Amicon Ultra-0.5 Centrifugal Filter Unit (Millipore#UFC500308) filters to completely remove the residual media. The resulting dispersion was sterile filtered through 0.22µm PVDF syringe filters (Cole-Parmer#UX-06060-62). OMVs were then characterized for size and size distribution using Dynamic Light Scattering (Zetasizer Nano ZS, Malvern Instruments). Protein concentration and OMVs were quantified with a Pierce™ BCA Protein Assay kit (Thermo Scientific), using BSA standards. Protein standards and OMVs were aliquoted and stored at –20°C.

Immunofluorescence microscopy

Immunofluorescence microscopy was used to investigate the presentation of nanobodies on the cell surface. A 200 μ L of nanobody expressing pInt-VHH72, pInt-Ty1, pLpp-OmpA-VHH72, and pLpp-OmpA-Ty1 recombinant bacterial cells were harvested and centrifuged at 3500 \times g for 5min and washed 3times with 1XPBS (pH7.4), supplemented with 3% BSA and incubated with recombinant Spike Protein (carrier-free Recombinant SARS-CoV-2 S Protein (S1+S2) (Bioline #793706)). Following three washes, Nanobody-Spike protein complex was added with anti-SARS-CoV-2 Protein S2 antibody (Bioline#943202) and incubated in dark for 1hr at RT. After washing 3 \times times with 1XPBS, nanobody-Spike-antibody complex was incubated 1.5hr at RT with anti-mouse IgG2 antibody conjugated with Alexa Fluor[®]647 (Bioline#406715). For microscopic observations, cells were washed 5 \times times with 1XPBS solution to remove unbound Alexa Fluor[®]647 antibody, then mounted on microscopic slide or in a 96-well plate and observed by fluorescence microscopy.

Antibody titer generation in response to oral administration of spike expressing EcN

All the animals used in these experiments were maintained in Association for the Assessment and Accreditation of Laboratory Animal Care approved facility (Assurance #D16-00190) in accordance with current regulations of the U.S. Department of Agriculture and Department of Health and Human Services. Experimental methods were approved in accordance with the institutional guidelines established by the Animal Care and Use Committee (approved protocol number: 20-05-16-01).

7–9-week-old male C57BL/6 mice ($n = 4-6$) purchased from Jackson Laboratories were used in all *in vivo* experiments. All core facilities are maintained specific-pathogen free. Animals were housed in HEPA-filtered micro insulator caging system at up to 4 animals per cage. All the animal experiments were conducted following a protocol

approved by The University of Cincinnati Biosafety, Radiation safety and Animal Care and Use Committees (20-05-16-01).

Engineered *EcN* cells were washed three times with 1XPBS with centrifugation at 3000 \times g for 5min and diluted in saline to 0.725, OD₆₀₀. For oral administration, mice were anesthetized using a 2% Isoflurane-air mixture. The anesthesia was maintained over the course of procedure using 1–1.5% isoflurane. Spike protein-expressing bacteria ($\sim 1 \times 10^7$ cfu) were orally administered in 6–9-week-old male C57BL6/J mice, every week for four consecutive weeks and their blood was withdrawn. Blood was spun at 2000 \times g for 30min at 4°C and serum was collected in an Eppendorf tube. Following administration, the mouse was returned to its original cage. For therapeutic assessment and bioluminescence imaging, each bacterial dose contained 1.0×10^7 bacteria suspended in saline. At the end point of the study, the mice were euthanized using Carbon dioxide inhalation and cervical dislocation, followed by collection of organs for further analysis.⁶¹

Mouse Anti-SARS-CoV-2 Antibody IgG Titer Serologic Assay Kit (Spike timer) was used to determine the antibody titer in the serum sample, according to the manufacturer's instructions (Acro Biosystems). In brief, 100 μ L of diluted serum sample, along with blank, positive, and negative control were added into a pre-coated SARS-CoV-2 Spike protein microplate and incubated at 37°C for 1hr. Following three washes with 1 \times washing buffer HRP-Goat anti-Mouse IgG was added and incubated at 37°C for 1hr in the dark. Following 3 \times washes, plate was added with 100 μ L substrate solution and incubated at 37°C for 20min, followed by termination of the reaction by adding 50 μ L of Stop solution. Absorbance was read at 450nm using UV/Vis's microplate spectrophotometer.

Vaccine (Moderna COVID-19 vaccine mRNA SpikevaxTM) and anti-spike monoclonal antibody (#KA6066, Abnova) were administered intramuscularly and intravenously, respectively. 1 μ g dose of vaccine and/or 1 μ g of monoclonal antibody was administered once in C57BL/6 male mice. EcN-Spike and EcN-Ty1 bacteria were given orally

(7×10^7 cfu) once. After 5 days of administration, mice were euthanized and blood, intestine, Bronchoalveolar lavage and feces were collected, aseptically. For BAL collection, animals were euthanized, and catheters were inserted via trachea following removal of salivary glands. 1XPBS was injected via the catheter and BAL was collected.⁶²

Live SARS-Cov-2 pseudovirus neutralizing antibody assay (Luciferase)

COVID-19 pseudovirus Neutralizing Antibody Assay (Luciferase) was performed as per the manufacturer's instructions (Abnova). In brief, prior to assay 293T-hACE2 cells ($\sim 1 \times 10^5$ cells/well) were grown in a 24 well plate and grown at 37°C for 4.00hr. Following incubation, media was removed, and cells were washed twice with 1XPBS. Cells were added with Cell Dissociation media (HIMEDIA) and incubated for 5min at 37°C and added with a complete medium to neutralize the reaction and centrifuged at $300 \times g$ for 5min. Pellet was resuspended in a complete medium to get 2×10^5 cells/mL. Meanwhile, 50 μ L diluted sample (OMV, Serum, antibody, or bacteria) and 10 μ L pseudovirus expressing luciferase were mixed and incubated at RT for 30min prior to adding to the 293T-hACE2 cells in a 24 well plate. Plates were incubated at 37°C for 48hr. Following incubation, medium was removed, and cells were gently washed with 200 μ L 1XPBS. It was added with 100 μ L of Luciferase Cell Lysis Reagent and cells were scrapped off the plate, vortexed for 10–15sec and centrifuged at $12,000 \times g$ for 30seconds and restored on ice instantly. 10 μ L of cell lysate and 50 μ L of Luciferase Assay Reagent were added in a 96-well plate and luminescence was immediately read using an *EnVision* 2102 Multilabel Reader (Perkin Elmer) to detect the Luciferase expression.

Bioluminescence imaging

Bioluminescence images were acquired using the Perkin Elmer's IVIS Spectrum *In Vivo* Imaging system (2 min exposure) for the quantification of Radiance (Photons/Sec/cm²) of the bioluminescent signals from the regions of interest.

Enzyme linked immunosorbent assay (ELISA)

ELISA for IgG (Thermo Fisher®), CD8⁺, CD4⁺ (MyBioSource®), and IgA (Raybiotech) were performed as per manufacturer's instructions.

Flow cytometry

Mice spleens were extracted and minced into 1mm pieces using a razor blade. The minced Spleens were washed three times with phosphate-buffered saline (PBS), to remove debris. The splenocytes were then suspended, in Hank's Balanced Salt Solution (HBSS) solution. Cell suspensions were filtered through a 70 μ m strainer, and RBCs were lysed using RBC Lysis buffer (Invitrogen), following the supplier's protocol. For immunophenotyping by flow cytometry, two million splenocytes per sample were used. The single cell suspensions were first labeled for 30 minutes at 4°C with LIVE/DEAD Fixable Blue (Invitrogen), to separate live cells from dead cells during analysis. After two washes, the samples were incubated for 30minutes at 4°C with the following antibodies: anti Mo CD3 super Bright 600 (eBiosciences 1782), anti-MO CD4 Brilliant violet 500 (eBioscience RM 4–5), anti-Mo CD8a-Super Bright 702 (eBioscience 53–6.7), anti-Mo CD56 AlexaFluor 588 (eBiosciences), anti-Mo-CD11c PE (eBiosciences N418), anti-Mo CD45 PerCpCyanine5.5 (eBiosciences 30-F11). After permeabilization, the samples were incubated with anti-MO CD68-Brilliant violet786 (eBioscience FA-11) for 30minutes at 4°C. Samples were analyzed on AttuneNXT (Thermo Fisher Scientific) flow cytometer. Unstained and single-stained samples were acquired and analyzed using FCS express (De Novo software).

Immunohistochemistry

Small and Large Intestines were isolated from the mice gut and fixed with 10%, v/v neutral buffered formalin for 24hr. It was replaced with storage solution 70%, v/v ethanol. Immunohistochemistry slides were prepared and developed by the Pathology Research Core at the Cincinnati Children's Hospital Medical Centre via the paraffin processing. These slides were imaged under x100 and x400 magnification using Leica DMI8

Widefield fluorescence/Brightfield Microscope. The images were quantified using ImageJ as previously reported.⁶³

Statistical analyses

All statistical analyses were performed using the GraphPad Prism 8.0.v. software. Ordinary one-way ANOVA was used to compare means between distinct groups, with at least 3 or more biological replicates and 2–3 experimental replicates. When two groups were compared two-tailed t-tests were used. Asterisks in the graphs represent that the mean differences were statistically significant ($p < 0.05$). The level of significance was set as “*” $p < 0.05$; “**” $p < 0.01$; “***” $p < 0.001$, ns- not significant.

Acknowledgments

We would like to thank Dr Ken Greis, Michael Wyder and Wendy Haffey from UC Proteomics Core for their help with Proteomics analysis. We also acknowledge the help from Betsy DiPasquale for preparing IHC and immunofluorescence samples, Chet Closson from Live Imaging core facility for the help with Fluorescent and Confocal Microscopic image acquisition, Xiangning Wang and Dr Lisa Lemen for assistance with IVIS Imaging, and the Laboratory Animal Medical Service Staff at The University of Cincinnati and the core facilities at the Cincinnati Children’s Hospital Medical Centre for the instrumental support. All schematics were constructed using BioRender and Inkscape.

Disclosure statement

NSK and NK have filed a patent application with the US patent and Trademark Office related to this work. All other authors declare no competing interests.

Funding

This work was supported by grants from NIH: R01HL168588, R01CA279962; CDMRP: ME200246; University of Cincinnati Office of Research and College of Pharmacy (to N.K.).

ORCID

Nalinikanth Kotagiri  <http://orcid.org/0000-0003-0066-4563>

Author contribution

N.K. conceived the project and with N.S.K. designed the experiments. All the experiments were lead and conducted by N.S.K. Further S.T., T.M., S.S., N.E., K.T., A.M. S. K. assisted with in vitro and animal studies. N.S.K. and N. K. analyzed the data and wrote the manuscript with feedback and review from all the authors.

Data availability statement

All the data generated or analyzed during this study are included in this article, supplemental information, and source files. Any additional information required to reanalyze the data reported in this paper is available from the lead contact upon request.

References

- Macpherson A, Harris N. Interactions between commensal intestinal bacteria and the immune system. *Nat Rev Immunol.* 2004;4(6):478–485. doi: [10.1038/nri1373](https://doi.org/10.1038/nri1373).
- Maslowski KM, MacKay CR. Diet, gut microbiota and immune responses. *Nat Immunol.* 2011;12(1):5–9. doi: [10.1038/ni0111-5](https://doi.org/10.1038/ni0111-5).
- Ichinohe T, Pang IK, Kumamoto Y, Peaper DR, Ho JH, Murray TS, Iwasaki A. Microbiota regulates immune defense against respiratory tract influenza A virus infection. *Proc Natl Acad Sci USA.* 2011;108(13):5354–5359. doi: [10.1073/pnas.1019378108](https://doi.org/10.1073/pnas.1019378108).
- Archambaud C, Nahori MA, Soubigou G, Bećavin C, Laval L, Lechat P, Smokvina T, Langella P, Lecuit M, Cossart P. Impact of lactobacilli on orally acquired listeriosis. *Proc Natl Acad Sci USA.* 2012;109(41):16684–16689. doi: [10.1073/pnas.1212809109](https://doi.org/10.1073/pnas.1212809109).
- Khailova L, Frank DN, Dominguez JA, Wischmeyer PE. Probiotic administration reduces mortality and improves intestinal epithelial homeostasis in experimental sepsis. *Anesthesiology.* 2013;119(1):166–177. doi: [10.1097/ALN.0b013e318291c2fc](https://doi.org/10.1097/ALN.0b013e318291c2fc).
- Isabella VM, Ha BN, Castillo MJ, Lubkowicz DJ, Rowe SE, Millet YA, Anderson CL, Li N, Fisher AB, West KA, et al. Development of a synthetic live bacterial therapeutic for the human metabolic disease phenylketonuria. *Nat Biotechnol.* 2018;36(9):857–864. doi: [10.1038/nbt.4222](https://doi.org/10.1038/nbt.4222).
- Galan JE, Wolf-Watz H. Protein delivery into eukaryotic cells by type III secretion machines. *Nature.* 2006;444(7119):567–573. doi: [10.1038/nature05272](https://doi.org/10.1038/nature05272).
- Pankiewicz VCS, Irving TB, Maia LGS, Ané JM. Are we there yet? The long walk towards the development of efficient symbiotic associations between nitrogen-fixing bacteria and non-leguminous crops. *BMC Biol.* 2019;17(1):1–17. doi: [10.1186/s12915-019-0710-0](https://doi.org/10.1186/s12915-019-0710-0).
- Vela Ramirez JE, Sharpe LA, Peppas NA. Current state and challenges in developing oral vaccines. *Adv Drug*

- Delivery Rev. 2017;114:116–131. doi: [10.1016/j.addr.2017.04.008](https://doi.org/10.1016/j.addr.2017.04.008).
10. New RRC. Formulation technologies for oral vaccines. *Clin Exp Immunol*. 2019;198(2):153–169. doi: [10.1111/cei.13352](https://doi.org/10.1111/cei.13352).
 11. Langel SN, Johnson S, Martinez CI, Tedjakusuma SN, Peinovich N, Dora EG, Kuehl PJ, Irshad H, Barrett EG, Werts AD, et al. Adenovirus type 5 SARS-CoV-2 vaccines delivered orally or intranasally reduced disease severity and transmission in a hamster model. *Sci Transl Med*. 2022;14(658):eabn6868. doi: [10.1126/scitranslmed.abn6868](https://doi.org/10.1126/scitranslmed.abn6868).
 12. Benbouziane B, Ribelles P, Aubry C, Martin R, Kharrat P, Riazi A, Langella P, Bermúdez-Humarán LG. Development of a stress-inducible controlled expression (SICE) system in *Lactococcus lactis* for the production and delivery of therapeutic molecules at mucosal surfaces. *J Biotechnol*. 2013;168(2):120–129. doi: [10.1016/j.jbiotec.2013.04.019](https://doi.org/10.1016/j.jbiotec.2013.04.019).
 13. Martín R, Martín R, Chain F, Chain F, Miquel S, Miquel S, Natividad JM, Natividad JM, Sokol H, Sokol H, et al. Effects in the use of a genetically engineered strain of *Lactococcus lactis* delivering in situ IL-10 as a therapy to treat low-grade colon inflammation. *Hum Vaccin Immunother*. 2014;10(6):1611–1621. doi: [10.4161/hv.28549](https://doi.org/10.4161/hv.28549).
 14. LeCureux JS, Dean GA, Papasian CJ. *Lactobacillus* mucosal vaccine vectors: immune responses against bacterial and viral antigens. *mSphere*. 2018;3(3):00061–18. doi: [10.1128/mSphere.00061-18](https://doi.org/10.1128/mSphere.00061-18).
 15. Huo J, Bas AL, Ruza RR, Duyvesteyn HME, Mikolajek H, Malinauskas T, Tan TK, Rijal P, Dumoux M, Ward PN, et al. Neutralizing nanobodies bind SARS-CoV-2 spike RBD and block interaction with ACE2. *Nat Struct & Mol Biol*. 2020;27(9):846–854. doi: [10.1038/s41594-020-0469-6](https://doi.org/10.1038/s41594-020-0469-6).
 16. Nambulli S, Xiang Y, Tilston-Lunel NL, Rennick LJ, Sang Z, Klimstra WB, Reed DS, Crossland NA, Shi Y, Paul Duprex W. Inhalable nanobody (PiN-21) prevents and treats SARS-CoV-2 infections in Syrian hamsters at ultra-low doses. *Sci Adv*. 2021;7(22):eabh0319. doi: [10.1126/sciadv.abh0319](https://doi.org/10.1126/sciadv.abh0319).
 17. Hanke L, Vidakovics Perez L, Sheward DJ, Das H, Schulte T, Moliner-Morro A, Corcoran M, Achour A, Karlsson Hedestam GB, Hällberg BM, et al. An alpaca nanobody neutralizes SARS-CoV-2 by blocking receptor interaction. *Nat Commun*. 2020;11(1):1–9. doi: [10.1038/s41467-020-18174-5](https://doi.org/10.1038/s41467-020-18174-5).
 18. Chanier T, Chames P. Nanobody engineering: toward next generation immunotherapies and immunoimaging of cancer. *Antibodies*. 2019;8(1):13. doi: [10.3390/antib8010013](https://doi.org/10.3390/antib8010013).
 19. Baud D, Dimopoulou Agri V, Gibson GR, Reid G, Giannoni E. Using probiotics to flatten the curve of coronavirus disease COVID-2019 Pandemic. *Front Public Heal*. 2020;8:1–5. doi: [10.3389/fpubh.2020.00186](https://doi.org/10.3389/fpubh.2020.00186).
 20. Sarnelli G, Del Re A, Pesce M, Lu J, Esposito G, Sanseverino W, Corpetti C, Basili Franzin S, Seguela L, Palenca I, et al. Oral immunization with *Escherichia coli* nissle 1917 expressing SARS-CoV-2 spike protein induces mucosal and systemic antibody responses in mice. *Biomolecules*. 2023;13(3):569. doi: [10.3390/biom13030569](https://doi.org/10.3390/biom13030569).
 21. Oberhettinger P, Schütz M, Leo JC, Heinz N, Berger J, Autenrieth IB, Linke D, Skurnik M. Intimin and invasins export their C-Terminus to the bacterial cell surface using an inverse mechanism compared to classical Autotransport. *PLOS ONE*. 2012;7(10):e47069. doi: [10.1371/journal.pone.0047069](https://doi.org/10.1371/journal.pone.0047069).
 22. Thomas SC, Madaan T, Kamble NS, Siddiqui NA, Pauletti GM, Kotagiri N. Engineered bacteria enhance immunotherapy and targeted therapy through stromal remodeling of tumors. *Adv Healthc Mater*. 2021;11(2):2101487. doi: [10.1002/adhm.202101487](https://doi.org/10.1002/adhm.202101487).
 23. Browning DF, Busby SJW. Local and global regulation of transcription initiation in bacteria. *Nat Rev Microbiol*. 2016;14(10):638–650. doi: [10.1038/nrmicro.2016.103](https://doi.org/10.1038/nrmicro.2016.103).
 24. Tillib SV, Ivanova TI, Vasilev LA, Rutovskaya MV, Saakyan SA, Gribova IY, Tutykhina IL, Sedova ES, Lysenko AA, Shmarov MM, et al. Isolation and characteristics of a new recombinant single domain antibody that specifically binds to human TNF. *Antiviral Research*. 2013;97(3):245–254. doi: [10.1016/j.antiviral.2012.12.014](https://doi.org/10.1016/j.antiviral.2012.12.014).
 25. Salema V, Fernández LÁ. *Escherichia coli* surface display for the selection of nanobodies. *Microb Biotechnol*. 2017;10(6):1468–1484. doi: [10.1111/1751-7915.12819](https://doi.org/10.1111/1751-7915.12819).
 26. Weikum J, Kulakova A, Tesei G, Yoshimoto S, Jägerum LV, Schütz M, Hori K, Skepö M, Harris P, Leo JC, et al. The extracellular juncture domains in the intimin passenger adopt a constitutively extended conformation inducing restraints to its sphere of action. *Sci Rep*. 2020;10(1):1–18. doi: [10.1038/s41598-020-77706-7](https://doi.org/10.1038/s41598-020-77706-7).
 27. Nicchi S, Giuliani M, Giusti F, Pancotto L, Maione D, Delany I, Galeotti CL, Brettoni C. Decorating the surface of *Escherichia coli* with bacterial lipoproteins: a comparative analysis of different display systems. *Microb Cell Fact*. 2021;20(1):1–14. doi: [10.1186/s12934-021-01528-z](https://doi.org/10.1186/s12934-021-01528-z).
 28. Earhart CF. Use of an Lpp-OmpA fusion vehicle for bacterial surface display. *Methods Enzymol*. 2000;326:506–516.
 29. Wendel S, Fischer EC, Martínez V, Seppälä S, Nørholm MHH. A nanobody: GFP bacterial platform that enables functional enzyme display and easy quantification of display capacity. *Microb Cell Fact*. 2016;15(1):1–13. doi: [10.1186/s12934-016-0474-y](https://doi.org/10.1186/s12934-016-0474-y).
 30. Jeiranikhameneh M, Razavi MR, Irani S, Siadat SD, Oloomi M. Designing novel construction for cell surface display of protein E on *Escherichia coli* using

- non-classical pathway based on lpp-OmpA. *AMB Express*. 2017;7(1):53. doi: [10.1186/s13568-017-0350-0](https://doi.org/10.1186/s13568-017-0350-0).
31. Cox J, Mann M. MaxQuant enables high peptide identification rates, individualized p.p.b.-range mass accuracies and proteome-wide protein quantification. *Nat Biotechnol*. 2008;26(12):1367–1372. doi: [10.1038/nbt.1511](https://doi.org/10.1038/nbt.1511).
 32. Hu Y, Liu C, Muyldermans S. Nanobody-based delivery systems for diagnosis and targeted tumor therapy. *Front Immunol*. 2017;8:1442. doi: [10.3389/fimmu.2017.01442](https://doi.org/10.3389/fimmu.2017.01442).
 33. Bao G, Tang M, Zhao J, Zhu X. Nanobody: a promising toolkit for molecular imaging and disease therapy. *EJNMMI Res*. 2021;11(1):6. doi: [10.1186/s13550-021-00750-5](https://doi.org/10.1186/s13550-021-00750-5).
 34. Schwechheimer C, Kuehn MJ. Outer-membrane vesicles from gram-negative bacteria: biogenesis and functions. *Nat Rev Microbiol*. 2015;13(10):605–619. doi: [10.1038/nrmicro3525](https://doi.org/10.1038/nrmicro3525).
 35. Arimilli S, Johnson JB, Clark KM, Graff AH, Alexander-Miller MA, Mizel SB, Parks GD. Engineered expression of the TLR5 ligand flagellin enhances paramyxovirus activation of human dendritic cell function. *J Virol*. 2008;82(22):10975–10985. doi: [10.1128/JVI.01288-08](https://doi.org/10.1128/JVI.01288-08).
 36. Gujrati V, Prakash J, Malekzadeh-Najafabadi J, Stiel A, Klemm U, Mettenleiter G, Aichler M, Walch A, Ntziachristos V. Bioengineered bacterial vesicles as biological nano-heaters for optoacoustic imaging. *Nat Commun*. 2019;10(1):1–10. doi: [10.1038/s41467-019-09034-y](https://doi.org/10.1038/s41467-019-09034-y).
 37. Cheng K, Zhao R, Li Y, Qi Y, Wang Y, Zhang Y, Qin H, Qin Y, Chen L, Li C, et al. Bioengineered bacteria-derived outer membrane vesicles as a versatile antigen display platform for tumor vaccination via Plug-and-display technology. *Nat Commun*. 2021;12(1):1–16. doi: [10.1038/s41467-021-22308-8](https://doi.org/10.1038/s41467-021-22308-8).
 38. Danaei M, Dehghankhold M, Ataei S, Davarani FH, Javanmard R, Dokhani A, Khorasani S, Mozafari MR. Impact of particle size and polydispersity index on the clinical applications of lipidic nanocarrier systems. *Pharmaceutics*. 2018;10(2):1–17. doi: [10.3390/pharmaceutics10020057](https://doi.org/10.3390/pharmaceutics10020057).
 39. Ronco C, Reis T, Husain-Syed F. Management of acute kidney injury in patients with COVID-19. *Lancet Respir Med*. 2020;8(7):738–742. doi: [10.1016/S2213-2600\(20\)30229-0](https://doi.org/10.1016/S2213-2600(20)30229-0).
 40. Glass DS, Riedel-Kruse IH. A synthetic bacterial cell-cell adhesion toolbox for programming multicellular morphologies and patterns. *Cell*. 2018;174(3):649–658.e16. doi: [10.1016/j.cell.2018.06.041](https://doi.org/10.1016/j.cell.2018.06.041).
 41. Prahlad J, Struble LR, Lutz WE, Wallin SA, Khurana S, Schnaubelt A, Broadhurst MJ, Bayles KW, Borgstahl GEO. CyDisCo production of functional recombinant SARS-CoV-2 spike receptor binding domain. *Protein Sci: A Publ Protein Soc*. 2021;30(9):1983–1990. doi: [10.1002/pro.4152](https://doi.org/10.1002/pro.4152).
 42. Velikova T, Mihova H, Kukov A, Snegarova V, Batselova A, Nakov R. Gastrointestinal mucosal immunity and covid-19. *World J Gastroenterol*. 2021;27(30):5047–5059. doi: [10.3748/wjg.v27.i30.5047](https://doi.org/10.3748/wjg.v27.i30.5047).
 43. Thursby E, Juge N. Introduction to the human gut microbiota. *Biochemical J*. 2017;474(11):1823–1836. doi: [10.1042/BCJ20160510](https://doi.org/10.1042/BCJ20160510).
 44. Hemarajata P, Versalovic J. Effects of probiotics on gut microbiota: mechanisms of intestinal immunomodulation and neuromodulation. *Therap Adv Gastroenterol*. 2013;6(1):39–51. doi: [10.1177/1756283X12459294](https://doi.org/10.1177/1756283X12459294).
 45. Kechagia M, Basoulis D, Konstantopoulou S, Dimitriadi D, Gyftopoulou K, Skarmoutsou N, Fakiri EM. Health benefits of probiotics: a review. *ISRN Nutr*. 2013;2013:1–7. doi: [10.5402/2013/481651](https://doi.org/10.5402/2013/481651).
 46. Gurbatri CR, Lia I, Vincent R, Coker C, Castro S, Treuting PM, Hinchliffe TE, Arpaia N, Danino T. Engineered probiotics for local tumor delivery of checkpoint blockade nanobodies. *Sci Transl Med*. 2020;12(530):eaax0876. doi: [10.1126/scitranslmed.aax0876](https://doi.org/10.1126/scitranslmed.aax0876).
 47. Stagg AJ. Intestinal dendritic cells in health and gut inflammation. *Front Immunol*. 2018;9:2883. doi: [10.3389/fimmu.2018.02883](https://doi.org/10.3389/fimmu.2018.02883).
 48. Bajaj V, Gadi N, Spihlman AP, Wu SC, Choi CH, Moulton VR. Aging, immunity, and COVID-19: how age influences the Host immune response to coronavirus infections? *Front Physiol*. 2021;11:1–23. doi: [10.3389/fphys.2020.571416](https://doi.org/10.3389/fphys.2020.571416).
 49. Pannu R, Dahiya S, Sabhlok VP, Kumar D, Sarsar V, Gahlawat SK. Effect of probiotics, antibiotics and herbal extracts against fish bacterial pathogens. *Ecotoxicol Environ Contam*. 2014;9(1):13–20. doi: [10.5132/eec.2014.01.002](https://doi.org/10.5132/eec.2014.01.002).
 50. Shi Y, Wang G, Peng Cai X, Wen Deng J, Zheng L, Hong Zhu H, Zheng M, Yang B, Chen Z. An overview of COVID-19. *J Zhejiang Univ Sci B*. 2020;21:343–360.
 51. Van Der Hooft JJJ, Goldstone RJ, Harris S, Burgess KEV, Smith DGE. Substantial extracellular metabolic differences found between phylogenetically closely related probiotic and pathogenic strains of *Escherichia coli*. *Front Microbiol*. 2019;10:252. doi: [10.3389/fmicb.2019.00252](https://doi.org/10.3389/fmicb.2019.00252).
 52. Leventhal DS, Sokolovska A, Li N, Plescia C, Kolodziej SA, Gallant CW, Christmas R, Gao JR, James MJ, Abin-Fuentes A, et al. Immunotherapy with engineered bacteria by targeting the STING pathway for anti-tumor immunity. *Nat Commun*. 2020;11(1):1–15. doi: [10.1038/s41467-020-16602-0](https://doi.org/10.1038/s41467-020-16602-0).
 53. Hosseini ZS, Amani J, Arani FB, Nazarian S, Motamedi MJ, Shafighian F. Immunogenicity of the nanovaccine containing intimin recombinant protein in the BALB/c mice. *Clin Exp Vaccine Res*. 2018;7(1):51–60. doi: [10.7774/cevr.2018.7.1.51](https://doi.org/10.7774/cevr.2018.7.1.51).
 54. Lieberman LA. Outer membrane vesicles: a bacterial-derived vaccination system. *Front Microbiol*. 2022;13:1–9. doi: [10.3389/fmicb.2022.1029146](https://doi.org/10.3389/fmicb.2022.1029146).

55. Chen P, Liu X, Sun Y, Zhou P, Wang Y, Zhang Y. Dendritic cell targeted vaccines: recent progresses and challenges. *Hum Vaccines Immunother.* **2016**;12(3):612–622. doi: [10.1080/21645515.2015.1105415](https://doi.org/10.1080/21645515.2015.1105415).
56. Matsuzaki T, Chin J. Modulating immune responses with probiotic bacteria. *Immunol Cell Biol.* **2000**;78(1):67–73. doi: [10.1046/j.1440-1711.2000.00887.x](https://doi.org/10.1046/j.1440-1711.2000.00887.x).
57. Wu HJ, Wu E. The role of gut microbiota in immune homeostasis and autoimmunity. *Gut Microbes.* **2012**;3(1):4–14. doi: [10.4161/gmic.19320](https://doi.org/10.4161/gmic.19320).
58. Oberhardt V, Luxemburger H, Kemming J, Schulien I, Ciminski K, Giese S, Csernalabics B, Lang-Meli J, Janowska I, Staniek J, et al. Rapid and stable mobilization of CD8⁺ T cells by SARS-CoV-2 mRNA vaccine. *Nature.* **2021**;597(7875):268–273. doi: [10.1038/s41586-021-03841-4](https://doi.org/10.1038/s41586-021-03841-4).
59. Zhang N, Li X, Deng Y, Wang Y, Ying B, Qin C, Zhang N, Li X, Deng Y, Zhao H, et al. Article a thermostable mRNA vaccine against COVID-19 || article a thermostable mRNA vaccine against COVID-19. *Cell.* **2020**;182(5):1271–1283.e16. doi: [10.1016/j.cell.2020.07.024](https://doi.org/10.1016/j.cell.2020.07.024).
60. Green CA, Kamble NS, Court EK, Bryant OJ, Hicks MG, Lennon C, Fraser GM, Wright PC, Stafford GP. Engineering the flagellar type III secretion system: improving capacity for secretion of recombinant protein. *Microb Cell Fact.* **2019**;18(1):10. doi: [10.1186/s12934-019-1058-4](https://doi.org/10.1186/s12934-019-1058-4).
61. Letran SE, Lee SJ, Atif SM, Uematsu S, Akira S, McSorley SJ. TLR5 functions as an endocytic receptor to enhance flagellin-specific adaptive immunity. *Eur J Immunol.* **2011**;41(1):29–38. doi: [10.1002/eji.201040717](https://doi.org/10.1002/eji.201040717).
62. Luckow B, Lehmann MH. A simplified method for bronchoalveolar lavage in mice by orotracheal intubation avoiding tracheotomy. *Biotechniques.* **2021**;71(4):534–537. doi: [10.2144/btn-2021-0022](https://doi.org/10.2144/btn-2021-0022).
63. Crowe A, Yue W. Semi-quantitative determination of protein expression using immunohistochemistry staining and analysis: an integrated protocol. *Bio-Protocol.* **2019**;9(24):1–11. doi: [10.21769/BioProtoc.3465](https://doi.org/10.21769/BioProtoc.3465).